

Metallicity evolution, metallicity gradients, and gas fractions at $z \sim 3.4^{*,**}$

P. Troncoso^{1,2}, R. Maiolino^{3,4}, V. Sommariva¹, G. Cresci⁵, F. Mannucci⁶, A. Marconi⁷, M. Meneghetti^{6,8}, A. Grazian¹,
A. Cimatti⁹, A. Fontana¹, T. Nagao^{10,11}, and L. Pentericci¹

¹ INAF – Osservatorio Astronomico di Roma, via di Frascati 33, 00040 Monte Porzio Catone, Italy
e-mail: troncoso@astro.rub.de

² Astronomisches Institut, Ruhr-Universität Bochum, Universitätsstraße 150, 44780 Bochum, Germany

³ Cavendish Laboratory, University of Cambridge, 19 J. J. Thomson Ave., Cambridge CB3 0HE, UK

⁴ Kavli Institute for Cosmology, University of Cambridge, Madingley Road, Cambridge CB3 0HA, UK

⁵ INAF – Osservatorio Astronomico di Bologna, via Ranzani 1, 40127 Bologna, Italy

⁶ INAF – Osservatorio Astrofisico di Arcetri, Largo E. Fermi 5, 50125 Firenze, Italy

⁷ Dip. di Fisica e Astronomia, Università di Firenze, via G. Sansone 1, 50019 Sesto F.no, Firenze, Italy

⁸ INFN, Sezione di Bologna, viale Berti Pichat 6/2, 40127 Bologna, Italy

⁹ Dipartimento di Fisica e Astronomia, Università di Bologna, via Ranzani 1, 40127 Bologna, Italy

¹⁰ The Hakubi Center for Advanced Research, Kyoto University, 606-8302 Kyoto, Japan

¹¹ Department of Astronomy, Kyoto University, Kitashirakawa-Oiwake-cho, Sakyo-ku, 606-8502 Kyoto, Japan

Received 18 June 2013 / Accepted 10 December 2013

ABSTRACT

We used near-infrared integral field spectroscopic observations from the AMAZE and LSD ESO programs to constrain the metallicity in a sample of 40 star-forming galaxies at $3 < z < 5$ (most of which are at $z \sim 3.4$). We measured metallicities by exploiting strong emission-line diagnostics. We found that a significant fraction of star-forming galaxies at $z \sim 3.4$ deviate from the fundamental metallicity relation (FMR), with a metallicity of up to a factor of ten lower than expected according to the FMR. This deviation does not correlate with the dynamical properties of the galaxy or with the presence of interactions. To investigate the origin of the metallicity deviation in more detail, we also inferred information on the gas content by inverting the Schmidt-Kennicutt relation, assuming that the latter does not evolve out to $z \sim 3.4$. In agreement with recent CO observational data, we found that in contrast with the steeply rising trend at $0 < z < 2$, the gas fraction in massive galaxies remains constant, with an indication of a marginal decline at $2 < z < 3.5$. When combined with the metallicity information, we infer that to explain the low metallicity and gas content in $z \sim 3.4$ galaxies, both prominent outflows and massive pristine gas inflows are needed. In ten galaxies we can also spatially resolve the metallicity distribution. We found that the metallicity generally anticorrelates with the distribution of star formation and with the gas surface density. We discuss these findings in terms of pristine gas inflows toward the center, and outflows of metal-rich gas from the center toward the external regions.

Key words. Galaxy: evolution – galaxies: high-redshift – galaxies: abundances – galaxies: star formation – galaxies: ISM – infrared: ISM

1. Introduction

Observations and theory have led during the past few years to a new scenario in which galaxy evolution is primarily regulated by the gas content in galaxies, which is, in turn, regulated by gas inflow and outflow phenomena. Millimeter observations have revealed large amounts of molecular gas in high-redshift galaxies (Tacconi et al. 2010; Daddi et al. 2010). These gas-rich galaxies are generally massive rotating disks, already in place at these early epochs, which obey the same Schmidt-Kennicutt star formation law (hereafter S-K law, Schmidt 1959; Kennicutt 1998) observed in the local Universe and whose enhanced star formation rate (SFR) is simply a consequence of their higher gas content relative to local galaxies and is not driven by enhanced

star formation efficiency (Genzel et al. 2004, 2010; Bouché et al. 2007; Daddi et al. 2010).

Several models can account for these observed trends. The emerging scenario is that at high redshift, gas from the intergalactic medium quickly replenishes galaxies through smooth cold flows (e.g. Dekel et al. 2009). As a consequence of the high pressure, this gas is mostly transformed into molecular hydrogen, which can effectively be used to feed star formation according to the models by Obreschkow & Rawlings (2009) and Lagos et al. (2011). These models provide a detailed description of the evolution of the molecular gas content in galaxies as a function of redshift and as a function of galaxy (halo) mass. According to these models, the evolution of the cosmic SFR is simply a consequence of the evolution of the molecular gas content in galaxies through the Schmidt-Kennicutt relation (Bouché et al. 2010; Genel et al. 2008).

Gas flows are thought to also be primarily responsible for the variation of metal contents in galaxies and their redshift

* Based on data obtained at the VLT through the ESO programs 178.B-0838, 075.A-0300 and 076.A-0711.

** Appendices are available in electronic form at <http://www.aanda.org>

evolution. In particular, the well-known mass–metallicity relation has been primarily ascribed to outflow of metal-rich gas, which is preferentially expelled from low-mass galaxies (Tremonti et al. 2004), although effects associated with the initial mass function (IMF), downsizing and gas infalls have also been invoked and several thorough theoretical models have been proposed (Köppen et al. 2007; Kobayashi et al. 2007; Brooks et al. 2007; De Rossi et al. 2007; Cescutti et al. 2007; Finlator & Davé 2008; Arrigoni et al. 2010; Calura & Menci 2009; Davé et al. 2011b, 2012; Sakstein et al. 2011; Dayal et al. 2013).

More recently, it has been found that the gas metallicity also has a secondary dependence on the SFR. At a given stellar mass the metallicity decreases with increasing SFR (Kewley 2006; Ellison et al. 2008; Mannucci et al. 2010; Lara Lopez et al. 2010; Cresci et al. 2012; Yates et al. 2012; Andrews & Martini 2013; Lilly et al. 2013; Pérez-Montero et al. 2013).

This three-dimensional relationship between stellar mass, SFR, and metallicity has been dubbed fundamental metallicity relation (FMR, Mannucci et al. 2010). This relation is very tight (dispersion 0.05 dex), suggesting that it reflects a smooth secular interplay between star formation and gas flows. In particular, one of the basic ideas behind the inverse correlation between SFR and metallicity is that it is primarily associated with inflow of pristine gas: the accreted gas on the one hand dilutes the gas metallicity, on the other hand boosts star formation through the Schmidt-Kennicutt relation. More detailed models and simulations have been presented by various authors to interpret the FMR (Davé et al. 2011b, 2012; Lagos et al. 2011; Yates et al. 2012; Dayal et al. 2013; Forbes et al. 2013).

Recently, by using spatially resolved spectroscopy of nearby galaxies, Sánchez et al. (2013) have not confirmed the metallicity dependence on the SFR, in contrast to previous studies. Part of the discrepancy may be associated with the use of the metallicity at the effective radius, instead of the metallicity obtained from the integrated line emission within the same aperture as used to infer the SFR. Indeed, Bothwell et al. (2013) have shown that the anticorrelation with the SFR (with low dispersion) is only found if both metallicity and SFR are extracted from the same aperture (and actually from the same spectrum integrated within the same aperture), while the scatter increases largely when the metallicity from the central region (SDSS fiber aperture) is compared with the total, integrated SFR. Bothwell et al. (2013) have also found evidence for a more fundamental relation between HI gas mass, metallicity, and stellar mass (HI-FMR). They suggested that the classical FMR (SFR-FMR) is a byproduct of the HI-FMR. However, even if the SFR-FMR were a consequence of the HI-FMR, the former can be considered as a tool for tracing galaxy evolutionary processes.

One important aspect of the FMR is that it is found not to evolve with redshift out to $z \sim 2.5$, suggesting that the same mechanism of galaxy formation is at work in most galaxies out to this redshift (Mannucci et al. 2010; Lara Lopez et al. 2010; Richard et al. 2011; Belli et al. 2013). Significant evolution was found at $z \sim 3$ by Mannucci et al. (2010) by using an initial subsample of the AMAZE (Assessing the Mass-Abundance redshift[Z] Evolution) and LSD (Lyman-break galaxies Stellar population and Dynamics) spectroscopic surveys (Maiolino et al. 2008; Mannucci et al. 2009). These authors found that galaxies at $z > 3$ are anomalously metal poor, specifically, about 0.6 dex below the FMR.

If the evolution of the FMR is confirmed at $z > 3$ with higher statistics, this may suggest a change in the dominant mode of galaxy formation. One possibility is that an excess of gas inflow at early epochs causes an excess of metallicity dilution.

Evidence for such massive inflows at $z \sim 3$ has been found through the analysis of metallicity gradients. By exploiting integral field spectroscopic data of three galaxies at $z \sim 3$ from the AMAZE sample, Cresci et al. (2010) found evidence for inverted (positive) metallicity gradients. In particular, the region of lowest metallicity was found to be coincident with the region of highest star formation, suggesting that strong inflow of pristine gas dilutes the metallicity and boosts star formation in these galaxies at $z \sim 3$. Studies of resolved metallicities at lower redshift have obtained mixed results, with samples of galaxies showing positive as well as negative gradients (Jones et al. 2010, 2013; Queyrel et al. 2012), possibly hinting at evolutionary trends and dependence on the dynamical status of galaxies. The inverted gradients at $z \sim 3$ are based on only three galaxies, hence requiring a larger sample to achieve a statistically sound result.

In this paper, we present the results from the full sample of $z \sim 3$ –4 galaxies from AMAZE, an ESO Large Program that exploits the VLT integral field near-IR spectrograph SINFONI (Spectrograph for INtegral Field Observations in the Near Infrared), combined with the parallel program LSD, performed with adaptive optics (AO), which are described in more detail in the next sections. While the dynamical properties of these samples were discussed in Gnerucci et al. (2011a), in this paper we focus on the distribution of the SFR (from which we inferred the gas fraction) and the metallicity properties (integrated and spatially resolved), by extending the results based on the first subsample presented in Maiolino et al. (2008), Mannucci et al. (2009), and Cresci et al. (2010).

2. AMAZE project: sample and data

This paper is primarily based on the AMAZE project, which uses near-IR integral field spectroscopy of star-forming galaxies at redshift $3 < z < 5$ with SINFONI (Eisenhauer et al. 2003) at the Very Large Telescope (VLT). A complete description of the AMAZE programs and of the methods used for data analysis and reduction are presented in Maiolino et al. (2008). Here we report a brief summary of the observing program and of the data obtained.

AMAZE is an ESO large program that was awarded 180 h of observations with SINFONI. The sample consists of 31 Lyman-break galaxies (LBGs) in the redshift range $3 < z < 5.2$ (most of which are at $z \sim 3.4$), with *Spitzer*/IRAC photometry (3.6 – $8 \mu\text{m}$) required to derive reliable stellar masses. Those LBGs that host AGNs were discarded based on either UV (optical rest-frame) spectra, hard X-ray data, or on the MIPS $24 \mu\text{m}$ flux (see discussion in Maiolino et al. 2008).

SINFONI was used in seeing-limited mode, with the $0.125'' \times 0.25''$ pixel scale and the H+K grating, yielding a spectral resolution $R \sim 1500$ over the spectral range 1.45 – $2.41 \mu\text{m}$. The typical seeing during the observations was about 0.6 – $0.7''$.

The main goals of the project are to obtain information on the metal enrichment and dynamics of galaxies at $z > 3$ by exploiting the optical nebular lines of [OII] $\lambda 3727$, [NeIII] $\lambda 3869$, H β , and [OIII] $\lambda \lambda 4959, 5007$ redshifted into the *H* and *K* bands.

Data were reduced by using the ESO-SINFONI pipeline (version 3.6.1). The pipeline subtracts the sky from the temporally contiguous frames, flat-fields the images, spectrally calibrates each individual slice, and then reconstructs the cube. Within the pipeline the pixels are resampled to a symmetric angular size of $0.125'' \times 0.125''$. The atmospheric absorption and

Table 1. Galaxy sample.

Object	Sample	RA	Dec	z	T_{exp} (min)	R_{AB}
CDFaC9	AMAZE	00:53:13.7	+12:32:11.1	3.2119	250	23.99
CDFS4414	AMAZE	03:32:23.2	-27:51:57.9	3.4714	350	24.18
CDFS4417 ¹	AMAZE	03:32:23.3	-27:51:56.8	3.4733	350	23.42
CDFS6664	AMAZE	03:32:33.3	-27:50:7.4	3.7967	500	24.80
CDFS16767	AMAZE	03:32:35.9	-27:41:49.9	3.6239	300	24.13
CDFS13497	AMAZE	03:32:36.3	-27:44:34.6	3.4138	150	24.21
CDFS11991	AMAZE	03:32:42.4	-27:45:51.6	3.6110	450	24.23
CDFS2528	AMAZE	03:32:45.5	-27:53:33.3	3.6872	350	24.64
CDFS16272	AMAZE	03:32:17.1	-27:42:17.8	3.6195	350	25.08
CDFS9313	AMAZE	03:32:17.2	-27:47:54.4	3.6545	250	24.82
CDFS9340 ¹	AMAZE	03:32:17.2	-27:47:53.4	3.6578	250	25.85
CDFS12631	AMAZE	03:32:18.1	-27:45:19.0	3.7090	250	24.72
CDFS14411	AMAZE	03:32:20.9	-27:43:46.3	3.5989	200	24.57
CDFS5161	AMAZE	03:32:22.6	-27:51:18.0	3.6610	300	24.96
LnA1689-2 ²	AMAZE	13:11:25.5	-01:20:51.9	4.8740	400	23.31
LnA1689-4 ²	AMAZE	13:11:26.5	-01:19:56.8	3.0428	240	22.40
LnA1689-1 ²	AMAZE	13:11:30.0	-01:19:15.3	3.7760	300	24.20
LnA1689-3 ^{2,4}	AMAZE	13:11:35.0	-01:19:51.6	5.120	225	25.0
Q1422D88	AMAZE	14:24:37.9	+23:00:22.3	3.7520	250	24.44
3C324C3	AMAZE	15:49:47.1	+21:27:05.0	3.2890	150	24.14
Cosmic Eye ^{2,3}	AMAZE	21:35:12.7	-01:01:42.9	3.0755	200	20.54
SSA22aM38	AMAZE	22:17:17.7	+00:19:00.7	3.2928	400	24.11
SSA22aC48 ⁴	AMAZE	22:17:18.6	+00:18:16.2	3.079	250	24.71
SSA22aD17 ¹	AMAZE	22:17:18.9	+00:18:16.8	3.0870	250	24.27
SSA22aang96M16	AMAZE	22:17:30.9	+00:13:10.7	3.2920	250	23.83
SSA22aG03 ⁴	AMAZE	22:17:30.8	+00:12:51.0	4.527	225	25.03
SSA22aC16	AMAZE	22:17:32.0	+00:13:16.1	3.0675	350	23.64
SSA22aC36	AMAZE	22:17:46.1	+00:16:43.0	3.0630	100	24.06
DFS2237bC21	AMAZE	22:39:29.0	+11:50:58.0	3.4029	200	23.50
DFS2237bD29	AMAZE	22:39:32.7	+11:55:51.7	3.3709	250	23.70
Q0302C131	LSD	03:04:35.0	-00:11:18.3	3.2350	240	24.5
Q0302C171	LSD	03:04:44.3	-00:08:23.2	3.3280	240	24.6
Q0302M80	LSD	03:04:45.7	-00:13:40.6	3.4160	240	24.1
Q0302MD287 ⁴	LSD	03:04:52.8	-00:09:54.6	2.395	160	24.8
SSA22aC30	LSD	22:17:19.3	+00:15:44.7	3.1025	240	24.2
SSA22aC6	LSD	22:17:40.9	+00:11:26.0	3.0970	280	23.4
SSA22aM4 ¹	LSD	22:17:40.9	+00:11:27.9	3.0972	280	24.8
SSA22bC5	LSD	22:17:47.1	+00:04:25.7	3.1120	240	22.0
DSF2237bD28	LSD	22:39:20.2	+11:55:11.3	2.9323	240	24.5
DSF2237bMD19 ⁴	LSD	22:39:21.1	+11:48:27.7	2.616	200	24.5

Notes. Column 1, object name; Col. 2, sample name, Cols. 3, 4, coordinates (J2000); Col. 5, redshift spectroscopically determined through the [OIII]5007 line in our spectra; Col. 6, on-source integration time (in unit of minutes); Col. 7, R band AB magnitude. ⁽¹⁾ The object is in the same field of view as the object on the previous line. ⁽²⁾ Lensed objects. ⁽³⁾ Data were taken from the archive. ⁽⁴⁾ Undetected sources. Redshift was taken from the literature.

instrumental response were taken into account and corrected for by using a suitable standard star.

In addition to *Spitzer* data, optical and near-IR photometry is available from the archives, see Steidel et al. (2003) and Grazian et al. (2006) and also from new observations (Sommariva et al. in prep.) obtained with the near-IR camera NICS (Baffa et al. 2001) mounted in the Telescopio Nazionale Galileo (TNG). *Hubble* Space Telescope (HST) optical and near-IR archival images (WFPC3, WFPC2, ACS) are available for most of the sources located in the GOODS-S survey field as well as for a few additional AMAZE targets in the archive. Of these we used primarily the images obtained with the filters *F606W*, *F775W*, and *F814W* to probe the rest-frame UV emission and, with this, study the environment and morphology (Sommariva et al., in prep.).

The full list of galaxies in the AMAZE sample along with some of their main observational properties is given in Table 1.

The AMAZE galaxies were extracted from the Steidel et al. (2003) and Vanzella et al. (2006) catalogs. The AMAZE sample ($\langle R \rangle \sim 24$) is globally representative of the galaxies in the parent samples (Steidel et al. 2003; Vanzella et al. 2006), which peak at $\langle R \rangle \sim 24.5$, although they are slightly brighter. Note that the galaxies were not pre-selected on any prior knowledge of nebular line detectability (either in the optical or in the near-IR).

In addition, five lensed galaxies were selected (marked with an asterisk in Table 1) that allowed us to probe galaxies with a lower SFR than that of the bulk of the sample. Four of these are lensed by the cluster Abell 1689, and their magnification factor was obtained by constructing a lens model of the cluster by using the 34 multiply imaged systems published in Limousin et al. (2007). Twenty-four of these multiply imaged systems have spectroscopic redshifts, which ensures that the model is robustly calibrated. To derive the cluster magnification maps, we used

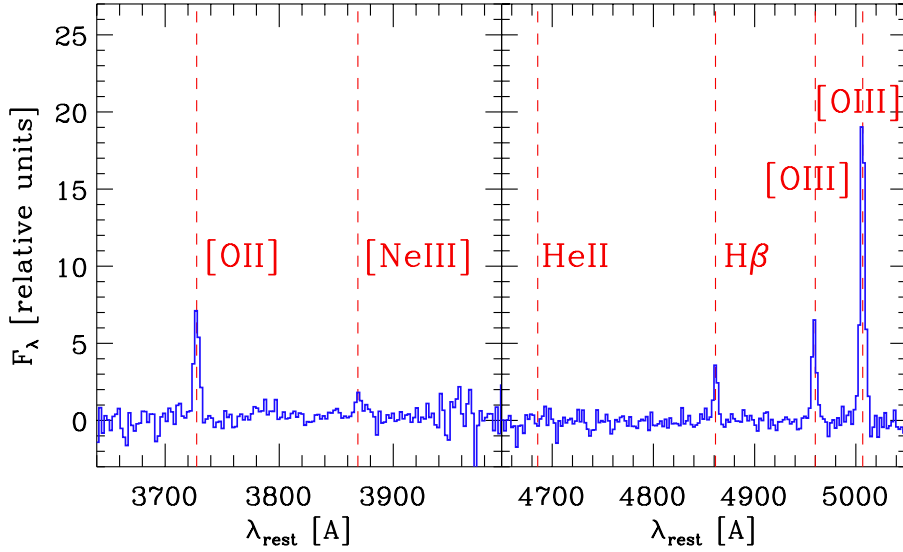


Fig. 1. Composite spectrum of the AMAZE and LSD spectra at $z \sim 3.4$ (34 sources). Note that a color version of all figures is available in electronic form.

the Lenstool public software (Kneib et al. 1996) and reproduced the Limousin et al. (2007) mass model using the parameter file¹. Then, we sampled the magnification maps to derive the local measurements of the magnification at the galaxy positions. The data for the fifth lensed source, the “Cosmic Eye”, were taken from the archive, and its magnification factor was taken from Smail et al. (2007).

Preliminary results on the mass–metallicity relation at $z \sim 3.4$ based on a first subset of nine galaxies are presented in Maiolino et al. (2008). As mentioned, the metallicity gradients for three bright and extended AMAZE galaxies are presented in Cresci et al. (2010). A study of the kinematics and dynamics of the whole sample is presented in Gnerucci et al. (2011a,b), who found a significant fraction (about one third) of galaxies to be characterized by regular disk-rotation patterns. Sommariva et al. (2012) also obtained stellar metallicities from optical (UV rest-frame) spectra of a few AMAZE galaxies, finding values broadly consistent with the metallicities inferred from the optical nebular lines.

3. LSD project

The AMAZE data are complemented with the LSD project, whose data are presented in Mannucci et al. (2009). LSD is a parallel SINFONI project consisting of observations assisted with the AO module of nine LBGs at $z \sim 3$. Data analysis and reduction are presented in Mannucci et al. (2009). Thanks to the exploitation of the AO module, these data achieve an angular resolution ($\sim 0.1\text{--}0.2''$) much higher than that of the AMAZE data.

The kinematics for the LSD galaxies is presented in Gnerucci et al. (2011a). HST data of the LSD galaxies is also available through new observations (Sommariva et al., in prep.).

The list of LSD galaxies is given in Table 1 along with their observational properties. The LSD sample is representative of the global LBG population selected by Steidel et al. (2003), as discussed in Mannucci et al. (2009).

4. Basic observational results

In this section we provide some basic observational results, such as the integrated spectra, integrated emission line fluxes, stacked spectra and ancillary data and information.

¹ Available at <http://www.astro.ku.dk/~marceau/model.par>

4.1. Emission lines

The spectra were extracted within fixed apertures of $0.75''$ in diameter (corresponding to ~ 5.4 kpc projected on sources at $z \sim 3.4$), which in most cases encloses more than 70% of the emission line flux and generally maximizes the signal-to-noise ratio (S/N). The same procedure was applied for the AMAZE and LSD sources previously published. There are four exceptions, SSA22aM38, SSA22aC36, CDFS12631, and DFS2237bC21, for which the line emission extends significantly beyond $0.75''$. Only for these four sources an aperture of $1.25''$ was used. Figures A.1–A.3, and A.5 show the spectra extracted for all unlensed sources.

For the three lensed sources at $z \sim 3$, LnA1689-1, LnA1689-4 and the Cosmic Eye the spectra were extracted manually by choosing high S/N regions. Their spectra are shown in Fig. A.4.

For all sources the redshift is such that [OII]3727 and [NeIII]3870 is redshifted into the H band, while $H\beta$ and [OIII]5007 are redshifted into the K band, with the exception of galaxies at $4.1 < z < 5.2$, for which only [OII] and [NeIII] are observable in the K band. Five sources are undetected, as noted in Table 1, two of which are at $z > 4$. CDFS13497 presents a very poor S/N spectrum (see Fig. A.2) and is excluded from the following analysis.

Figure 1 shows the stacked spectrum of all sources at $z < 4$. It is important to note that the stacked spectrum shows no evidence for the HeII nebular line at $\lambda 4686 \text{ \AA}$. This line is expected if there is contribution from AGNs. The nondetection of this line additionally supports that our selection criteria carefully excluded AGNs from the sample.

The emission lines fluxes were obtained by fitting the emission lines with Gaussian functions by imposing the same full width at half maximum for all the lines within the same band (hence with the same instrumental resolution, which slightly changes with wavelength). To automatically exclude noise fluctuations or bad pixels we constrained the velocity dispersion of the lines to be higher than the instrumental resolution estimated from the sky emission lines. The continuum, when detected (marginally), was subtracted with a simple linear slope, and the uncertainties in the subtraction were included in the final errors on the line fluxes. In Table 2 the measured emission line fluxes are reported. As mentioned, out of the 40 galaxies in the joint AMAZE+LSD sample, 34 have detections of all emission lines required to infer the metallicity.

Table 2. Line fluxes inferred from the near-IR spectra.

Name	$F([\text{OIII}]5007)$	$F(\text{H}\beta)$	$F([\text{OII}]3727)$	$F([\text{NeIII}]3870)$
	$10^{-17} \text{ erg s}^{-1} \text{ cm}^{-2}$			
CDFaC9	7.23 \pm 0.09	1.49 \pm 0.09	2.36 \pm 0.11	0.60 \pm 0.09
CDFS4414	1.06 \pm 0.08	0.42 \pm 0.06	0.89 \pm 0.08	0.12 \pm 0.04
CDFS4417	1.77 \pm 0.08	0.88 \pm 0.09	1.39 \pm 0.09	0.31 \pm 0.07
CDFS6664	3.38 \pm 0.15	0.34 \pm 0.09	0.29 \pm 0.04	–
CDFS16767	1.99 \pm 0.08	0.46 \pm 0.09	0.60 \pm 0.05	–
CDFS11991	3.02 \pm 0.10	0.28 \pm 0.09	0.52 \pm 0.05	0.22 \pm 0.07
CDFS2528	1.61 \pm 0.11	0.35 \pm 0.10	0.61 \pm 0.07	–
CDFS16272	3.62 \pm 0.09	0.48 \pm 0.13	0.66 \pm 0.05	0.23 \pm 0.09
CDFS9313	4.45 \pm 0.13	0.54 \pm 0.12	0.72 \pm 0.06	–
CDFS9340	1.64 \pm 0.10	0.37 \pm 0.09	0.40 \pm 0.06	–
CDFS12631	2.98 \pm 0.25	0.49 \pm 0.12	2.09 \pm 0.19	1.13 \pm 0.13
CDFS14411	3.88 \pm 0.13	0.75 \pm 0.11	1.02 \pm 0.07	0.20 \pm 0.06
CDFS5161	1.23 \pm 0.17	0.17 \pm 0.09	0.17 \pm 0.04	0.11 \pm 0.05
LnA1689-2 ^a	–	–	0.16 \pm 0.03	0.05 \pm 0.03
LnA1689-4 ^a	0.45 \pm 0.01	0.05 \pm 0.00	0.06 \pm 0.01	0.02 \pm 0.00
LnA1689-1 ^a	0.15 \pm 0.02	0.04 \pm 0.01	0.06 \pm 0.01	–
Q1422D88	4.31 \pm 0.21	0.55 \pm 0.17	0.55 \pm 0.08	–
3C 324C3	1.15 \pm 0.08	0.26 \pm 0.06	0.46 \pm 0.12	0.31 \pm 0.11
Cosmic Eye ^a	0.78 \pm 0.02	0.09 \pm 0.03	0.24 \pm 0.03	–
SSA22aM38	5.56 \pm 0.14	1.40 \pm 0.18	3.12 \pm 0.18	1.03 \pm 0.16
SSA22aD17	1.73 \pm 0.11	0.36 \pm 0.09	1.04 \pm 0.10	–
SSA22aag96M16	1.82 \pm 0.08	0.38 \pm 0.06	0.47 \pm 0.08	–
SSA22aC16	5.45 \pm 0.09	1.47 \pm 0.12	2.59 \pm 0.09	–
SSA22aC36	1.81 \pm 0.24	0.48 \pm 0.21	2.12 \pm 0.32	0.34 \pm 0.17
DSF2237bC21	0.70 \pm 0.12	1.00 \pm 0.17	1.85 \pm 0.14	0.35 \pm 0.13
DSF2237bD29	0.93 \pm 0.09	0.14 \pm 0.07	0.76 \pm 0.09	–
Q0302C131	2.62 \pm 0.52	0.46 \pm 0.16	0.80 \pm 0.32	–
Q0302C171	1.10 \pm 0.12	0.18 \pm 0.08	0.56 \pm 0.24	–
Q0302M80	1.32 \pm 0.26	0.40 \pm 0.12	0.56 \pm 0.18	–
SSA22aC30	1.28 \pm 0.22	0.26 \pm 0.10	0.30 \pm 0.12	–
SSA22aC6	5.50 \pm 0.62	0.76 \pm 0.45	1.21 \pm 0.38	–
SSA22aM4	3.66 \pm 0.49	0.69 \pm 0.25	1.46 \pm 0.23	–
SSA22bC5	3.28 \pm 0.24	0.50 \pm 0.14	0.27 \pm 0.09	0.38 \pm 0.14
DSF2237bD28	1.86 \pm 0.36	0.16 \pm 0.08	0.74 \pm 0.16	–
<i>Composite</i> ^b	6.13 \pm 0.14	1.00 \pm 0.10	1.70 \pm 0.12	0.39 \pm 0.08

Notes. Column 1, object name; Cols. 2–5, emission line fluxes. ^(a) Values corrected for a magnification factor of 5.9 ± 1.9 , 43.5 ± 4.1 , 6.7 ± 2.1 (see text), and 28 ± 3 (Smail et al. 2007), respectively. ^(b) In the case of the composite spectrum fluxes were normalized to the H β flux (which is also subject to an error, as listed in the corresponding column).

As pointed out in Gnerucci et al. (2011a), many of the sources in the seeing-limited AMAZE data and the AO-assisted LSD are spatially resolved. A detailed study on the morphology and size determination by using different methods of the AMAZE and LSD galaxies will be published in a companion work (see Sommariva et al., in prep.). In general, the different methods used to determine the size are inconsistent with each other, with differences ranging up to a factor of four or more. This questions the reliability of the size determination and, even more importantly, its meaning. This has implications for the determination of the surface brightness of galaxies, as discussed in more detail below (see Sect. 6).

4.2. Physical properties determined from the broad-band SED

For each galaxy in our sample a multiwavelength broad-band spectral energy distribution (SED) was built with published or

archival data and was fitted with a set of galaxy spectral templates to obtain the stellar mass, SFR, age, and dust reddening. The broad-band photometric data for the sources in the CDFS were collected from the GOODS-MUSIC multiwavelength catalog (Grazian et al. 2006). This catalog provides photometric data in 14 spectral bands (from UV to the *Spitzer*-IRAC bands) and has recently been updated to include the *Spitzer*-MIPS data at 24 μm . For the LBGs extracted from the Steidel et al. (2003) sample, optical photometric data (U , G , R , I) were extracted from the publicly available images (Steidel et al. 2003), while *Spitzer* IRAC and MIPS data were obtained from the *Spitzer* archive or from new observations (Mannucci et al. 2009); the photometry extraction was performed following the same methods described in Grazian et al. (2006).

The galaxy templates and best-fitting technique are the same as those used in previous papers (Grazian et al. 2006, 2007), and similar to those adopted by other groups in the literature (e.g. Dickinson et al. 2003; Drory et al. 2004; Pozzetti et al. 2007).

Table 3. Physical properties of the sample inferred from their SED and metallicity.

Name	$\log M_*$ (BC03) [M_\odot]	$\log M_*$ (M05) [M_\odot]	$E(B - V)_*$ [mag]	$\log SFR$ (SED) [$M_\odot \text{ yr}^{-1}$]	$\log SFR$ (H β) [$M_\odot \text{ yr}^{-1}$]
CDFaC9	9.95 ^{+0.40} _{-0.08}	9.90 ^{+0.30} _{-0.05}	0.00	2.19 ^{+0.18} _{-0.30}	1.65 ^{+0.14}
CDFS4414	10.35 ^{+0.19} _{-0.23}	10.25 ^{+0.07} _{-1.24}	0.20	1.82 ^{+0.25} _{-0.62}	1.80 ^{+0.31}
CDFS4417	10.07 ^{+0.38} _{-0.11}	10.09 ^{+0.12} _{-0.05}	0.25	2.41 ^{+0.01} _{-0.63}	2.33 ^{+0.31}
CDFS6664	9.26 ^{+0.11} _{-0.23}	9.07 ^{+0.22} _{-0.08}	0.10	1.31 ^{+0.27} _{-0.31}	1.36 ^{+0.33}
CDFS16767	9.82 ^{+0.10} _{-0.16}	9.67 ^{+0.13} _{-0.13}	0.15	1.69 ^{+0.31} _{-0.05}	1.67 ^{+0.31}
CDFS11991	9.47 ^{+0.13} _{-0.16}	9.42 ^{+0.18} _{-0.08}	0.10	1.51 ^{+0.26} _{-0.24}	1.23 ^{+0.34}
CDFS2528	9.54 ^{+0.09} _{-0.08}	9.48 ^{+0.16} _{-0.00}	0.20	1.77 ^{+0.02} _{-0.33}	1.77 ^{+0.33}
CDFS16272	8.97 ^{+0.18} _{-0.08}	9.00 ^{+0.19} _{-0.09}	0.10	1.22 ^{+0.02} _{-0.30}	1.46 ^{+0.33}
CDFS9313	9.29 ^{+0.29} _{-0.28}	9.29 ^{+0.25} _{-0.27}	0.10	1.27 ^{+0.29} _{-0.63}	1.54 ^{+0.32}
CDFS9340	8.86 ^{+0.39} _{-0.28}	8.85 ^{+0.32} _{-0.26}	0.10	0.84 ^{+0.29} _{-0.65}	1.37 ^{+0.32}
CDFS12631	9.97 ^{+0.45} _{-0.10}	10.18 ^{+0.10} _{-0.29}	0.30	2.17 ^{+0.05} _{-0.86}	2.34 ^{+0.32}
CDFS14411	9.28 ^{+0.08} _{-0.03}	9.30 ^{+0.05} _{-0.05}	0.15	1.62 ^{+0.05} _{-0.02}	1.88 ^{+0.31}
CDFS5161	9.65 ^{+0.58} _{-0.24}	9.67 ^{+0.29} _{-0.24}	0.20	1.59 ^{+0.27} _{-1.21}	1.43 ^{+0.40}
LnA1689-2 ^a	9.88 ^{+0.21} _{-0.36}	9.79 ^{+0.10} _{-0.32}	0.06	1.14 ^{+0.18} _{-0.30}	1.31 ^{+0.34}
LnA1689-4 ^a	8.46 ^{+0.26} _{-0.39}	8.12 ^{+0.53} _{-0.03}	0.06	0.10 ^{+0.18} _{-0.30}	0.04 ^{+0.24}
LnA1689-1 ^a	9.91 ^{+0.06} _{-0.10}	9.63 ^{+0.21} _{-0.09}	0.00	0.38 ^{+0.18} _{-0.30}	0.09 ^{+0.19}
Q1422D88	10.60 ^{+0.02} _{-0.23}	10.43 ^{+0.11} _{-0.10}	0.00	0.94 ^{+0.30} _{-0.05}	1.36 ^{+0.19}
3C324C3	9.67 ^{+0.33} _{-0.23}	9.62 ^{+0.28} _{-0.16}	0.20	1.72 ^{+0.25} _{-0.95}	1.53 ^{+0.32}
Cosmic Eye ^a	9.55 ^{+0.48} _{-0.48}	9.55 ^{+0.48} _{-0.48}	0.40	1.67 ^{+0.40} _{-0.40}	1.63 ^{+0.36}
SSA22aM38	10.78 ^{+0.18} _{-0.41}	10.48 ^{+0.19} _{-0.40}	0.20	1.83 ^{+0.18} _{-0.30}	2.27 ^{+0.31}
SSA22aD17	9.95 ^{+0.50} _{-0.61}	9.67 ^{+0.50} _{-0.27}	0.10	1.42 ^{+0.18} _{-0.30}	1.18 ^{+0.32}
SSA22aaug96M16	10.06 ^{+0.20} _{-0.21}	9.92 ^{+0.11} _{-0.28}	0.06	1.39 ^{+0.18} _{-0.30}	1.20 ^{+0.24}
SSA22aC16	10.61 ^{+0.13} _{-0.55}	10.46 ^{+0.11} _{-0.37}	0.35	2.58 ^{+0.18} _{-0.30}	2.84 ^{+0.31}
SSA22aC36	10.10 ^{+0.30} _{-0.20}	10.08 ^{+0.21} _{-0.17}	0.25	2.06 ^{+0.27} _{-1.46}	1.91 ^{+0.38}
DSF2237bC21	10.80 ^{+0.14} _{-0.31}	10.55 ^{+0.06} _{-0.11}	0.06	1.44 ^{+0.74} _{-0.56}	1.65 ^{+0.24}
DSF2237bD29	10.72 ^{+0.15} _{-0.22}	10.55 ^{+0.14} _{-0.11}	0.00	1.35 ^{+0.50} _{-0.56}	0.66 ^{+0.26}
Q0302C131 [*]	10.09 ^{+0.10} _{-0.33}	–	0.15	1.11 ^{+0.16} _{-0.26}	1.00 ^{+0.22} _{-0.40}
Q0302C171 [*]	10.06 ^{+0.10} _{-0.28}	–	0.10	1.00 ^{+0.13} _{-0.18}	0.70 ^{+0.40} _{-0.40}
Q0302M80 [*]	10.07 ^{+0.23} _{-0.19}	–	0.30	1.54 ^{+0.26} _{-0.70}	1.11 ^{+0.12} _{-0.21}
SSA22aC30 [*]	10.33 ^{+0.31} _{-0.38}	–	0.40	2.00 ^{+0.29} _{-1.35}	1.46 ^{+0.14} _{-0.45}
SSA22aC6 [*]	9.68 ^{+0.15} _{-0.06}	–	0.40	1.73 ^{+0.16} _{-0.24}	1.36 ^{+0.32} _{-0.46}
SSA22aM4 [*]	9.41 ^{+0.34} _{-0.13}	–	0.40	1.33 ^{+0.27} _{-0.89}	1.30 ^{+0.30} _{-0.19}
SSA22bC5 [*]	8.96 ^{+0.38} _{-0.22}	–	0.25	0.93 ^{+0.23} _{-0.52}	1.18 ^{+0.00} _{-0.27}
DSF2237bD28 [*]	9.78 ^{+0.28} _{-0.29}	–	0.30	1.33 ^{+0.25} _{-0.66}	1.15 ^{+0.11} _{-0.24}

Notes. Column 1, object name; Col. 2, stellar mass inferred from the galaxy templates of BC03; Col. 3, stellar mass inferred from the galaxy templates of M05; Col. 4, dust reddening that affects the stellar light, from the attenuation curve of Calzetti et al. (2000); Col. 5, star formation rate (from BC03); Col. 6, star formation rate (from H β flux). To compare our results with other studies using the Chabrier IMF, the masses and the star formation rates were calculated from the Salpeter IMF corrected for a factor of 1.7. The stellar mass, reddening, and star formation rate of the Cosmic Eye correspond to the best-fitting SED values reported in Coppin et al. (2007), the SFR(H β) was derived with the measured H β flux, and the reported extinction considering an error of ± 0.15 mag. ^(a) Values corrected for a magnification factor of 43.5 ± 4.1 , 6.7 ± 2.1 , 5.9 ± 1.9 (see text), and 28 ± 3 (Smail et al. 2007), respectively. ^(*) LSD galaxies, all values have been taken from Mannucci et al. (2009).

The galaxy templates were computed with standard spectral synthesis models (Bruzual & Charlot 2003, hereafter BC03) and were chosen to broadly encompass the variety of star formation histories, ages, metallicities, and extinction of real galaxies. More specifically, we considered an exponentially declining SFR with e -folding times ranging from 0.1 to 15 Gyr. We used the Salpeter IMF ($M_{\min} = 0.1 M_\odot$ and $M_{\max} = 65 M_\odot$), ranging over a set of metallicities (from $Z = 0.02 Z_\odot$ to $Z = 2.5 Z_\odot$) and dust extinction ($0 < E(B - V) < 1.1$), with a Calzetti et al. (2000) attenuation curve, which is generally more appropriate for the

stellar component. For each model of this grid, the expected magnitudes were computed in the desired filter sets (depending on the available public data). The best-fitting template was found with a standard χ^2 minimization. The stellar mass and other physical parameters of the galaxy, such as SFR, age, and dust extinction, were fitted simultaneously to the actual SED of the observed galaxy. To compare our results with other studies, using the Chabrier IMF, we applied a correction factor of 1.7 (Pozzetti et al. 2007) to our masses and SFR. The SED-fitting results are reported in Table 3. For the four lensed sources masses and

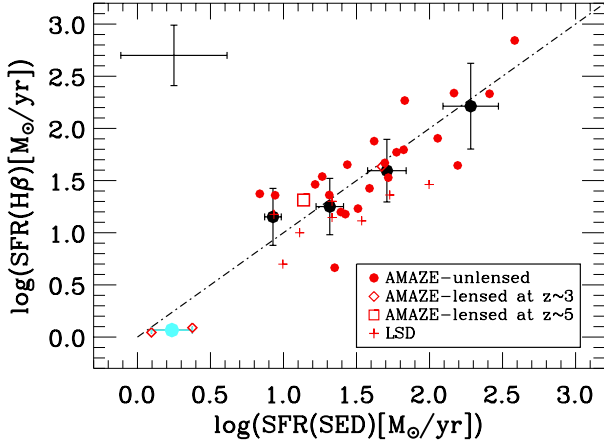


Fig. 2. Comparison between the SFRs derived from the SED fitting and the SFR based on $H\beta$. The dashed line shows the 1:1 relation along which the two estimators agree perfectly. The red circles are unlensed AMAZE galaxies at $z \sim 3.4$. The red diamonds are the three lensed sources at $z \sim 3.4$. The red empty square is the lensed galaxy at $z = 4.8$ for which $H\beta$ emission has been inferred from $[OII]\lambda 3727$ by assuming the $[OII]/H\beta$ ratio appropriate for its metallicity (see Appendix B). The red crosses show the LSD galaxies. Black filled circles show the $SFR(H\beta)$ averaged within bins of $SFR(SED)$. The cyan bin is composed of the two lensed galaxies LnA1689-1 and LnA1689-4. The error bars on the binned values correspond to the dispersion of the SFR within each bin. The error bars in the top-left corner indicate the average uncertainties on the measurements of $SFR(SED)$ and $SFR(H\beta)$ for the individual objects.

SFR were corrected for the magnification factor obtained by us (Ln1689-1, Ln1689-2, Ln1689-4) or in the literature (Cosmic Eye, Smail et al. 2007), as reported in Table 3.

4.3. Star formation rates

The SFR can also be inferred also from the $H\beta$ line flux that, if unreddened, is proportional to the number of ionizing photons emitted by young hot stars.

We inferred the SFR from $H\beta$ by first correcting for it through the reddening inferred from the continuum-fitting, then by applying a stellar-to-nebular differential correction factor of 1/0.44, as discussed in Calzetti et al. (2000) (although the applicability of this correction factor for high redshift galaxies is subject to some debate, as discussed in Reddy et al. 2012). We finally obtained the $H\alpha$ luminosity by assuming the case-B recombination, that is, $H\alpha/H\beta = 2.8$, and by adopting the $H\alpha$ to SFR conversion factor given by Kennicutt (1998). The errors of the flux measurements presented in Table 2 and the reddening ($\Delta(E(B - V)) = 0.1$) were taken into account to derive the final $SFR(H\beta)$ presented in Table 3. Uncertainties in $SFR(H\beta)$ are at a one-sigma level. We note that the correction for the $H\beta$ flux for stellar absorption is negligible. Indeed, the continuum is not detected, or barely detected, in all of the spectra; therefore, even assuming that the $H\beta$ stellar absorption on the continuum is as deep as it can be (e.g. post-starburst A-type-like spectra), this would not change the inferred $H\beta$ flux by more than a few percent.

Figure 2 shows the comparison between the SFR inferred from the SED with the SFR inferred from $H\beta$, where, for the sake of clarity, we averaged the data in bins of $SFR(SED)$ and where the error bars give the dispersion of the points in each bin. Each bin has seven galaxies on average, except for the cyan symbol, which has two galaxies. The latter shows the average obtained

from the two lensed sources LnA1689-1 and LnA1689-4, which allowed us to explore low SFRs. The error bars in the top-right corner show the average measurement on individual objects. There is a good general agreement between the two tracers of star formation over the two orders of magnitude spanned by our data. A more extensive discussion of the reliability and a comparison of the different SFR tracers for the galaxies in our sample is given in a companion paper, Castellano et al. (2013). In the following we used (unless stated otherwise) the SFR inferred from $H\beta$ ($SFR_{H\beta}$), but the results are essentially unchanged if one uses the SFR inferred from the SED.

5. Metallicity evolution

In this section we investigate the integrated metallicity of the LBG galaxies at $z \sim 3-5$, its dependence on stellar mass and SFR, and compare them with lower-redshift galaxies to infer possible evolutionary effects.

To infer the metallicities we adopted the same method as in Maiolino et al. (2008) and in Mannucci et al. (2009). Essentially, the method consists of exploiting the R_{23} parameter (where $R_{23} = (F([OII]\lambda 3727) + F([OIII]\lambda 4959) + F([OIII]\lambda 5007))/F(H\beta)$, which depends on metallicity. The dependence of this parameter on the metallicity has been calibrated by various authors, either by using theoretical models or through empirical calibrations based on other primary indicators (such as the electronic temperature T_e inferred from auroral lines). A summary of some of the calibrations is given in Kewley & Ellison (2008). Maiolino et al. (2008) adopted a hybrid calibration method, in which at low metallicities ($12 + \log(O/H) < 8.4$, where models have problems in reproducing the observed line ratios) the R_{23} parameter is calibrated directly through the T_e method, while at high metallicities ($12 + \log(O/H) > 8.4$, where the electron temperature is more difficult to measure and subject to temperature fluctuations) the calibration is obtained by exploiting models. The main problem with the R_{23} parameter is that it has a double metallicity solution for each value (upper and lower branches). Maiolino et al. (2008) selected the branch through the $[NeIII]\lambda 3869/[OII]\lambda 3727$ and $[OIII]\lambda 5007/[OII]\lambda 3727$ ratios. These are tracers of the ionization parameter, but also depend monotonically on the metallicity (although with large scatter), meaning that the ionization parameter correlates, on average, with the metallicity. In practice, we simultaneously fitted the three diagnostics and found the best solution. A more detailed discussion on the method adopted to infer the metallicities is given in Appendix B. Although the use of this method brings with it some caveats, it was also adopted in Mannucci et al. (2010) and thus allows a direct comparison with the results in that work (FMR).

Finally, for the one lensed AMAZE galaxy at $z = 4.8$, for which we can only observe $[NeIII]$ and $[OII]$ in the K band, we inferred the metallicity from the $[NeIII]/[OII]$ line ratio, exploiting the anticorrelation (though with high dispersion) between this line ratio and the metallicity found in Maiolino et al. (2008). In Table 4 the integrated metallicities inferred for the AMAZE and LSD galaxies are reported.

5.1. Mass–metallicity relation at $z \sim 3.4$

Figure 3 shows the mass–metallicity relation for the full AMAZE+LSD sample. In the left panel the red symbols show the individual measurements of the AMAZE and LSD galaxies. Red points denote the AMAZE unlensed sources, diamonds the AMAZE lensed sources at $z \sim 3$, and the red square shows the

Table 4. Galaxy mass estimated using OIII images. Derived quantity yields and metallicities.

Name	$\log M_{\text{gas}}(\Sigma\text{SFR}) M_{\odot}$	Gas fraction	$12 + \log(\text{O}/\text{H})$	log Yields
CDFaC9	9.51 ± 0.29	0.27 ± 0.17	$8.07^{+0.17}_{-0.17}$	-2.61 ± 0.54
CDFS4414	10.11 ± 0.30	0.37 ± 0.20	$8.47^{+0.11}_{-0.10}$	-2.09 ± 0.50
CDFS4417	10.47 ± 0.30	0.72 ± 0.18	$8.48^{+0.09}_{-0.09}$	-1.60 ± 0.62
CDFS6664	9.61 ± 0.30	0.69 ± 0.17	$7.88^{+0.17}_{-0.20}$	-2.25 ± 0.72
CDFS16767	9.49 ± 0.30	0.32 ± 0.16	$8.28^{+0.20}_{-0.32}$	-2.34 ± 0.69
CDFS11991	9.47 ± 0.30	0.50 ± 0.19	$7.87^{+0.20}_{-0.20}$	-2.53 ± 0.68
CDFS2528	9.97 ± 0.30	0.73 ± 0.14	$8.22^{+0.24}_{-0.31}$	-1.84 ± 0.87
CDFS16272	9.30 ± 0.30	0.68 ± 0.16	$7.92^{+0.23}_{-0.23}$	-2.22 ± 0.77
CDFS9313	9.87 ± 0.30	0.79 ± 0.16	$7.95^{+0.23}_{-0.25}$	-1.97 ± 0.83
CDFS9340	9.89 ± 0.30	0.91 ± 0.08	$8.28^{+0.14}_{-0.71}$	-1.23 ± 1.18
CDFS12631	10.31 ± 0.30	0.69 ± 0.20	$7.89^{+0.16}_{-0.17}$	-2.25 ± 0.69
CDFS14411	9.72 ± 0.30	0.73 ± 0.14	$8.16^{+0.23}_{-0.28}$	-1.89 ± 0.74
CDFS5161	9.87 ± 0.30	0.62 ± 0.27	$7.69^{+0.37}_{-0.39}$	-2.54 ± 0.93
LnA1689-2	10.09 ± 0.31	0.62 ± 0.23	$7.92^{+0.74}_{-0.11}$	-2.32 ± 1.42
LnA1689-4	9.17 ± 0.29	0.84 ± 0.14	$7.92^{+0.11}_{-0.11}$	-1.89 ± 0.66
LnA1689-1	9.58 ± 0.30	0.32 ± 0.16	$8.35^{+0.19}_{-0.26}$	-2.27 ± 0.66
Q1422D88	9.63 ± 0.30	0.10 ± 0.07	$7.94^{+0.24}_{-0.33}$	-2.99 ± 0.71
3C324C3	9.80 ± 0.30	0.57 ± 0.23	$7.79^{+0.35}_{-0.29}$	-2.51 ± 0.91
Cosmic Eye	9.63 ± 0.29	0.55 ± 0.32	$7.97^{+0.32}_{-0.23}$	-2.37 ± 0.81
SSA22aM38	10.14 ± 0.30	0.19 ± 0.15	$8.14^{+0.11}_{-0.15}$	-2.64 ± 0.45
SSA22aD17	9.40 ± 0.30	0.22 ± 0.25	$8.24^{+0.18}_{-0.17}$	-2.50 ± 0.54
SSA22aAug96M16	9.33 ± 0.30	0.16 ± 0.11	$8.21^{+0.18}_{-0.60}$	-2.62 ± 0.95
SSA22aC16	10.81 ± 0.29	0.61 ± 0.24	$8.35^{+0.13}_{-0.15}$	-1.90 ± 0.62
SSA22aC36	10.01 ± 0.30	0.45 ± 0.22	$8.44^{+0.13}_{-0.15}$	-2.02 ± 0.57
DSF2237bC21	10.08 ± 0.30	0.16 ± 0.11	$8.79^{+0.08}_{-0.07}$	-2.04 ± 0.36
DSF2237bD29	9.85 ± 0.30	0.12 ± 0.09	$8.34^{+0.19}_{-0.19}$	-2.55 ± 0.52

Notes. Column 1, object name; Col. 2, mass of gas in [M_{\odot}] obtained by inverting the Schmidt-Kennicutt law and adding the surface star formation rate at every galaxy pixel throughout the galaxy extension; Col. 3, gas fraction; Col. 4, metallicity at 0.375 arcsec using the [Maiolino et al. \(2008\)](#) metallicity calibration; Col. 5, effective yields.

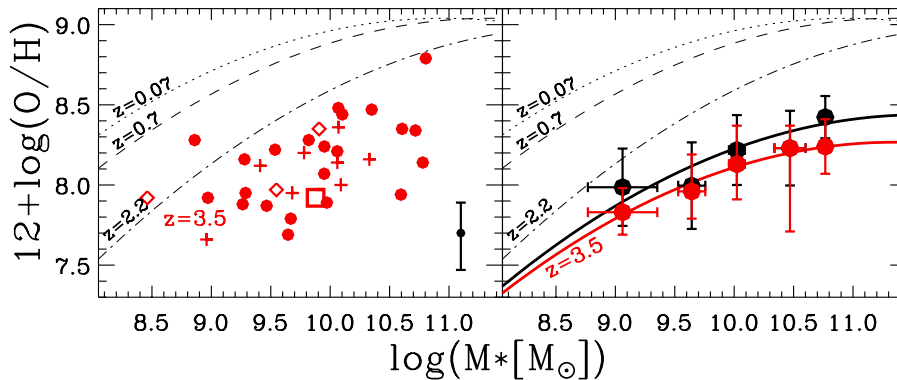


Fig. 3. Mass-metallicity relation for the galaxies in the AMAZE and LSD samples. The *left panel* shows the individual AMAZE and LSD galaxies at $z \sim 3$ – 5 (same symbol codes as in Fig. 2). The overplotted lines (dotted, dashed, dot-dashed) shows the mass–metallicity relation at lower redshifts from previous studies ($z \sim 0.07$, 0.7 , and 2.2 respectively, see [Maiolino et al. \(2008\)](#)). The average error bar on the metallicity determination is shown in the lower-right corner. In the *right panel* the data are binned according to stellar mass. The black circles show the average metallicities within each stellar mass bin, while the red circles show the metallicity inferred from the spectra stacked in the same bins. The solid black line shows the fit to the average metallicities, while the red solid line shows the fit to the metallicity of the stacked spectra.

lensed source at $z \sim 5$. Red crosses are the LSD sources. In the right panel, the full sample at $3 < z < 3.7$ is binned according to stellar mass in intervals of 0.5 dex. The black points show the average metallicities in each stellar mass bin, while the red circles show the metallicity inferred from the spectra stacked in the same bins. Each bin has six galaxies on average. The overplotted curves are the best fits of the observed mass–metallicity relations at different redshifts obtained by various previous surveys (see [Maiolino et al. \(2008\)](#)). Over the investigated mass range, the metallicity at $z \sim 3.4$ is about 0.8 dex lower than for local

galaxies. For the best fit to the mass–metallicity relation, we adopted the same description of the mass–metallicity relation as in [Maiolino et al. \(2008\)](#),

$$12 + \log(\text{O}/\text{H}) = -0.0864 (\log M_* - \log M_0)^2 + K_0, \quad (1)$$

where $\log M_0$ and K_0 were determined at each redshift to obtain the best fit to the observed data points. By using the complete AMAZE+LSD sample at $z \sim 3.4$, we obtained $\log M_0 = 11.35, 11.59$ and $K_0 = 8.27, 8.44$ for the stacked and average

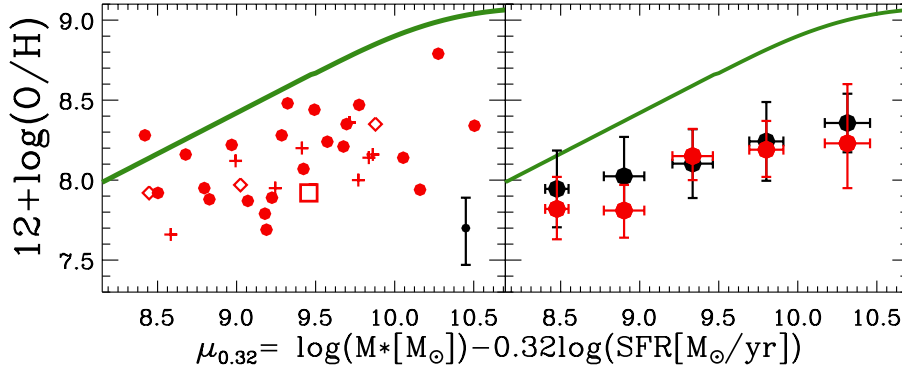


Fig. 4. Metallicity as a function of the parameter $\mu_{0.32}$. The green line plots the FMR projection as a function of $\mu_{0.32}$ (Mannucci et al. 2011). The *left panel* shows the individual AMAZE and LSD galaxies at $z \sim 3-5$ (same symbol codes as in Fig. 2). The average metallicity uncertainty of the sample is shown in the lower-right corner. In the *right panel* the data are binned by the $\mu_{0.32}$ parameter. The black circles show the average metallicities in each $\mu_{0.32}$ bin, while the red circles show the metallicity of the spectra stacked in the same bins. The black error bars show the dispersion of the average metallicity and $\mu_{0.32}$ at each bin. The vertical red error bars show the error of the metallicity of the stacked spectrum in each bin. The horizontal red error bars show the dispersion of the average $\mu_{0.32}$ in each bin.

metallicities, respectively². The inclusion of low-mass systems ($\log M_* < 9.5 M_\odot$), with respect to Maiolino et al. (2008), results in a flatter relation than at lower redshifts. However, this putative evolution of the mass–metallicity evolution is still convolved with the different SFRs probed at different redshifts by the different surveys. Since the metallicity of galaxies also depends on their SFR, as discussed in Mannucci et al. (2010), the evolution of the mass–metallicity relation with redshift (both in normalization and shape) is largely apparent and mostly due to the higher SFR of galaxies observed at high redshift (both because of selection effects and because of the real intrinsic evolution of the average SFR in galaxies). Therefore, it is more meaningful to investigate the metallicity evolution relative the three-dimensional relation that involves stellar mass as well as SFR, as discussed in the next section.

5.2. Evolution at $z \sim 3.4$ compared with the fundamental metallicity relation

As we mentioned in Sect. 1, Mannucci et al. (2010) have observationally shown that galaxies in the redshift range $0 < z < 2.5$ are described by a tight three-dimensional relation between stellar mass (M_*), SFR and gas-phase metallicity. The homogeneity of the FMR in the redshift range $0 < z < 2.5$ suggests that the mechanisms that drive the galaxy evolution during this time interval are similar. A deviation of galaxies from the FMR at higher redshift (at $z \gtrsim 2.5$) would indicate different evolutionary mechanisms at such early epochs.

At $z \sim 3$ Mannucci et al. (2010) analyzed a subsample of 17 AMAZE and LSD galaxies and found a deviation of the *average* metallicity of these galaxies from the FMR (at $0 < z < 2.5$) of about -0.6 dex.

In our sample, the metallicity of the full AMAZE+LSD composite spectrum at $z \sim 3.4$ (34 galaxies) is $8.03^{+0.16}_{-0.18}$, this is $0.43^{+0.16}_{-0.18}$ dex lower than the expected metallicity from the FMR (8.46) evaluated at the average star formation ($10^{1.5} M_\odot \text{yr}^{-1}$) and average stellar mass ($10^{9.8} M_\odot$) of the full sample. The aim of this section is to investigate the behavior of the full AMAZE+LSD sample at $z \sim 3.4$ (twice the size of that used by Mannucci et al. 2010) compared with the FMR, by investigating the deviations as a function of SFR and mass through

exploiting the fact that the 34 galaxies of the sample span over two orders of magnitude in mass and SFR.

To further quantify the deviations of the data at $z \sim 3.4$ with respect to the local/low- z FMR, we used the parameter $\mu_{0.32} = \log(M_*) - 0.32 \log(\text{SFR})$, which provides a projection of the FMR that minimizes the metallicity scatter of local galaxies (Mannucci et al. 2010) and its extension to the lower masses of Mannucci et al. (2011). This projection of the FMR shows the deviation of $z \sim 3.4$ galaxies compared with to the local FMR more clearly and more globally.

In Fig. 4, the green line is the best fit of the metallicity distribution of local galaxies as a function of $\mu_{0.32}$ (see Mannucci et al. 2011). In the left panel, the individual measurements of the full AMAZE+LSD sample are shown (same symbol-coding as in Fig. 3). Galaxies at $z \sim 3.4$ have a metallicity dispersion of about 0.25 in dex, much higher than local galaxies (which have $\sigma \sim 0.05$), which probably reflects the mixture of different stages of unsteady chemical evolutionary processes at this epoch, in contrast to what is observed at later epochs.

In the right panel, the black circles show the average metallicities in $\mu_{0.32}$ bins, while the red symbols show the metallicity of the stacked spectra in the same bins. The plot also shows that the deviation from the FMR increases as a function of $\mu_{0.32}$. This trend is more clearly shown in Fig. 5, where we plot the deviation of $z \sim 3$ galaxies (averaged and stacked in bins of $\mu_{0.32}$, black and red points, respectively) as a function of $\mu_{0.32}$.

The deviations (up to 0.6–1 dex) are clearly much higher than the mean scatter of local galaxies on the FMR (~ 0.05 dex). For comparison, in Fig. 5 we also show the location of galaxies at $z \sim 0.25-0.65$ (Cresci et al. 2012), at $z \sim 1$ (Vergani et al. 2012), and at $z \sim 2$ (Law et al. 2009; Lehnert et al. 2009), whose average metallicities are derived with the Maiolino et al. (2008) calibration for consistency. Galaxies at $z \sim 0.25-0.65$ do not show any deviation compared with the local FMR. Galaxies at $z \sim 1-2$ do show some marginal deviation from the FMR at high μ_{32} , but it is much lower than that of galaxies at $z > 3$. This result indicates that the deviation from the FMR is mostly a peculiarity of $z > 3$ galaxies, which suggests a transition epoch across $z \sim 3$ where the main mode of galaxy formation probably changes.

To better understand the physical parameters that drive the deviations at $z \sim 3.4$ from the FMR, we also investigated the dependence of the deviations from FMR as a function of other galaxy physical parameters. In particular, we investigated the deviation of $z \sim 3.4$ galaxies from the FMR as a function of stellar

² To avoid the fit to be dominated by the mass intervals with the largest number of objects, we first obtained the metallicity average or stacked within mass bins and then fitted the resulting values with Eq. (1).

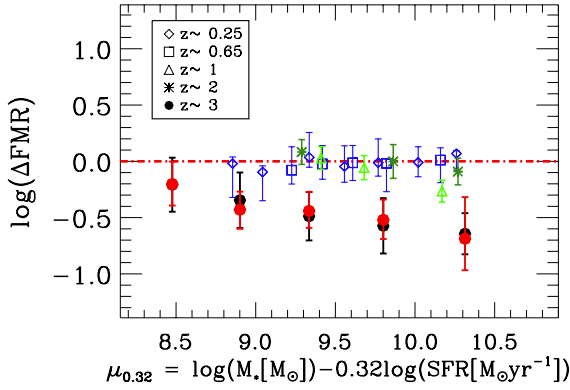


Fig. 5. Deviation of the FMR as a function of the $\mu_{0.32}$ parameter. Black and red circles show metallicity differences of the averaged and stacked spectra, respectively, within each $\mu_{0.32}$ bin compared with the FMR. The black error bars show the dispersion of the average metallicity within each bin. The red error bars show the error of the metallicity of the stacked spectrum in each bin. Blue diamonds, blue squares, green triangles, and green asterisks show the average metallicity differences compared with the FMR of galaxies at $z \sim 0.25, 0.65, 1,$ and $2,$ respectively (Cresci et al. 2012; Vergani et al. 2012; Law et al. 2009; Lehnert et al. 2009).

mass, SFR, and specific SFR ($sSFR = SFR/M_*$, which is a proxy of the evolutionary stage of galaxies). None of these parameters strongly correlate with the deviation from the FMR, the main driving quantity of the deviations is the μ_{32} parameter that, as discussed in Mannucci et al. (2010), is linked to the star formation efficiency and to the combined effect of inflows and outflows. We investigate these scenarios in more detail in Sect. 7.

A possible origin of the deviation of galaxies at $z \sim 3.4$ from the FMR may be associated with an increased rate of mergers, which destabilize low-metallicity gas in galaxy outskirts and drive it toward the central, active regions, as suggested by some models (e.g. Rupke et al. 2010; Perez et al. 2011; Pilkington et al. 2012; Torrey et al. 2012).

The dynamical properties of the AMAZE+LSD sample has been studied by Gnerucci et al. (2011a). They found a significant fraction ($\sim 30\%$) of galaxies with regular rotation, especially among massive systems, indicating that massive rotating disks (although highly turbulent) were already in place at this early epoch. Other galaxies show irregular kinematics, suggesting recent or ongoing merging, while for other galaxies it is not possible to distinguish between rotation or irregular kinematics due to low angular resolution or low S/N.

Figure 6 shows the distribution of the metallicity difference from the FMR of galaxies at $z \sim 3.4$. We divided the sample between rotating and nonrotating systems (according to Gnerucci et al. 2011a). There is no significant difference between rotating and nonrotating systems in terms of deviations from the FMR; the average deviation from the FMR of rotating systems is $\langle \log(\Delta FMR) \rangle = -0.37^{+0.27}_{-0.36}$, while the average deviation of nonrotating systems is $\langle \log(\Delta FMR) \rangle = -0.58^{+0.23}_{-0.08}$. We also divided the sample into interacting and isolated galaxies by visual inspection of the available HST images (including those in the H band). There is no significant difference between interacting and isolated systems in terms of deviations from the FMR; the average deviation from the FMR of isolated systems is $\langle \log(\Delta FMR) \rangle = -0.29^{+0.10}_{-0.28}$, while the average deviation of interacting systems is $\langle \log(\Delta FMR) \rangle = -0.37^{+0.26}_{-0.36}$. These results suggests that enhanced merging cannot be the only explanation for the deviation from the FMR in galaxies at $z \sim 3.4$. Moreover,

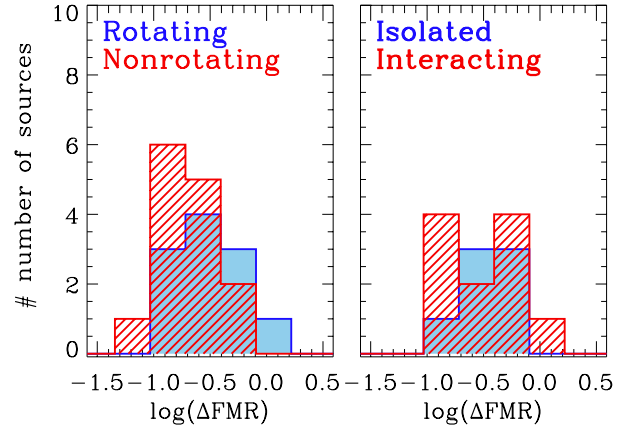


Fig. 6. Histogram of the metallicity deviations from the FMR for the AMAZE and LSD galaxies at $z \sim 3.4$. The blue histograms refer to the rotating disks and isolated galaxies. The red histograms indicate the non-rotating galaxies and interacting galaxies.

there are indications that merging galaxies in the local Universe are following the FMR (Cresci et al., in prep.).

Another possibility is that the deviation from the FMR at $z > 3$ is associated with selection effects and, in particular, with the color-selection criterion of LBG galaxies. The color selection tends to avoid dusty galaxies, which are presumably more metal rich. However, other samples at lower redshifts were color-selected, but do not show similar strong deviations from the FMR, as discussed above. Moreover, some of the most deviating galaxies are also the most massive, which should also be the most dusty (according to the mass-dust relation observed locally and at high redshift), which contrasts with the putative color bias. Therefore, the deviation from the FMR seems to be a peculiarity intrinsic to $z > 3$ galaxies.

While a discussion of the potential physical scenarios that might explain the deviations of galaxies at $z > 3$ is given in Sects. 7 and 8, we note here that gas metallicities are not the only property that indicates a transition in galaxy evolution at $z \sim 3$. Indeed, the finding that galaxies at $z > 3$ deviate from the trends observed at lower redshift has also been obtained in other studies. Moller et al. (2013) have found an indication for a transition in the metal content of DLA at $z \sim 2.6$, which they interpreted as a transition from an epoch dominated by strong gas infall to the more quiescent, later epoch in terms of gas accretion. A transition at a similar epoch has also been observed in the reddening properties of Ly α emitters and QSO host galaxies (Fynbo et al. 2013; Nilsson & Moller 2009, 2011; Bongiovanni et al. 2010).

Even more interesting, Prochaska & Wolfe (2009) have shown that the HI content in galaxies does not evolve in the redshift range $0 < z < 2.5$, while it does evolve at higher redshifts. They associated the transition phase with the conversion of HI into H₂ at $z < 2.5$, which in turn regulates star formation and metal production. Although additional modeling is required, it is clear that our result suggesting a transition of galaxy evolution occurring at $z \sim 2.5-3.0$ is in line with various other observational results.

There is yet another possibility to explain the deviation of our sample at $z \sim 3.4$ from the FMR: LBGs at high- z might belong to a different class of objects that, at any redshift, do not obey the FMR. Hunt et al. (2012) have shown that low-mass, low-metallicity galaxies follow a “fundamental plane”, whose extension to high masses falls short to account for star-forming disks observed in the SDSS, but does reproduce the

properties of the LBG at high- z . It is not simple to directly compare our results with the result of [Hunt et al. \(2012\)](#), since they used different metallicity tracers and so the comparison may be subject to significant offsets introduced by the different calibrations adopted for the different samples (see [Kewley & Ellison 2008](#)). Moreover, the sample adopted by [Hunt et al. \(2012\)](#) tends to preferentially select low-metallicity galaxies, and the stellar mass estimation is also different from ours. Finally, [Hunt et al. \(2012\)](#) used the AMAZE and LSD galaxies (the previous subsample of 17 galaxies) to construct the relationship, which makes claiming a consistency of the AMAZE+LSD sample with the work of [Hunt et al. \(2012\)](#) is somewhat circular. However, the scenario of a nonevolving population of strongly star-forming galaxies that deviates from the FMR is a scenario that should be investigated in more detail by including additional independent samples.

6. Gas content

As we discuss in the next sections, to properly interpret the metallicity evolution in galaxies, it is extremely useful to have information on the gas content. This additional information allows us to partly remove degeneracies between various scenarios (e.g., closed-box, inflows, outflows). However, with the exclusion of a few powerful SMGs and QSO host galaxies, the direct measurement of the gas content in galaxies at $z > 3$ is still extremely challenging and, so far, only a few detections have been obtained ([Riechers et al. 2010](#); [Magdis et al. 2012a](#)), only one of which (the Cosmic Eye) overlaps with our sample. An alternative method used by various authors (e.g. [Conselice et al. 2013](#); [Vergani et al. 2012](#); [Tan et al. 2013](#); [Erb et al. 2006b](#); [Mannucci et al. 2009](#)) to infer the gas content, is to invert the S-K law although this is indirect and subject to larger uncertainties.

In the local Universe, the S-K law relates the gas surface density (Σ_{gas}) with the star-formation surface density (Σ_{SFR} , [Schmidt 1959](#); [Kennicutt 1998](#); [Bigiel et al. 2008](#); [Schruba et al. 2011](#)). Recently, [Genzel et al. \(2010\)](#), [Daddi et al. \(2010\)](#), [Tacconi et al. \(2010\)](#), [Tacconi et al. \(2013\)](#), and [Saintonge et al. \(2013\)](#) have measured large amounts of molecular gas in star-forming disks at $z \sim 1-2.7$ and have found that the S-K law was already in place even at those early epochs of the Universe. Similar results have been obtained by using the dust mass as a proxy of the gas content in high- z galaxies ([Magdis et al. 2012b](#); [Santini et al. 2014](#)).

Therefore, the currently favored scenario is that the high SFRs measured at $z \sim 1-2.7$ are caused by the large amount of molecular gas and not by a more efficient mechanism that converts gas into stars.

If the AMAZE galaxies are considered as typical star-forming disks at $z \sim 3$ (i.e., assuming the validity of the S-K law), and assuming that the S-K relation does not evolve³ out to $z \sim 3$, we can infer the Σ_{gas} from the Σ_{SFR} , and finally derive the gas mass. A similar approach was adopted by [Erb et al. \(2006b\)](#) and [Vergani et al. \(2012\)](#) for galaxies at $z \sim 1.5$, by [Conselice et al. \(2013\)](#) at $z \sim 1.5-3$, and by [Mannucci et al. \(2009\)](#) for galaxies at $z \sim 3$. Most of these previous studies do not really map the Σ_{SFR} ; instead, they measure a “size” of the galaxies and infer an average Σ_{SFR} by dividing the total SFR

by the average “size” of the galaxy, and from this they derive an average Σ_{gas} . By following this method, assuming an idealized galaxy with a constant Σ_{SFR} within a radius r (by using the S-K law and adopting a Chabrier IMF), we obtain the relation

$$\Sigma_{\text{gas}}(M_{\odot}/\text{pc}^2) = 241 \left(\frac{\text{SFR}}{M_{\odot}/\text{yr}} \right)^{0.71} \left(\frac{r}{\text{kpc}} \right)^{-1.42} \quad (2)$$

and

$$M_{\text{gas}}(M_{\odot}) = 757 \times 10^6 \left(\frac{\text{SFR}}{M_{\odot}/\text{yr}} \right)^{0.71} \left(\frac{r}{\text{kpc}} \right)^{0.58}, \quad (3)$$

where SFR is the total galaxy SFR. A factor of 1.7 between the Salpeter (adopted in [Kennicutt 1998](#)) and Chabrier IMF was applied ([Pozzetti et al. 2007](#)).

However, this method is subject to two main caveats. First, the previous equations are formally correct for a disk with a flat, constant distribution of Σ_{SFR} within a radius r . It is not obvious that for a distribution of Σ_{SFR} typical of star-forming galaxies (especially those at $z \sim 3$) these equations are appropriate, especially given that the S-K relation is not linear. Secondly, it is not clear which galaxy radius should be used to infer the average Σ_{SFR} : as we have discussed in the previous section, the galaxy radius may change by even a factor of several, depending on the method adopted to determine the radius and on the adopted definition of “galaxy radius”. In galaxies with irregular morphologies (e.g., multiple knots) or interacting/merging systems it is even more unclear which radius should be taken.

Here we adopted a different method that is much less affected by these problems. We measured the Σ_{SFR} within each individual pixel and from this derived the Σ_{gas} locally by applying the S-K relation, and the gas mass sampled by each pixel by simply multiplying the local Σ_{gas} by the physical area sampled by the pixel. We then inferred the total gas mass by simply combining the gas masses inferred in each pixel. This method is rigorous when the galaxy is fully resolved. It totally bypasses all problems associated with the radius definition, irregular morphologies, and interacting systems that affect the previous method. Obviously, when the galaxy is not resolved or is only marginally resolved, this method incurs problems similar to the previous one. However, as discussed below, for the class of galaxies observed by us, which are resolved, we have tested that our new method provides a much more accurate determination of the gas content.

We simulated galaxies with different Sersic profiles, different effective radii ($R_e = 0.5, 1., 1.5, 2., 2.5$ kpc), and different Sersic indices ($n = 0.5, 1, 2, 3, 4$). We also simulated interacting/merging systems by combining two of the previously simulated galaxies, separated by 1 to 2 kpc. These simulated images describe the true (intrinsic) distribution of Σ_{SFR} and, by inverting the S-K law, we can derive the true distribution of Σ_{gas} and therefore the true gas mass. Then, these images were smoothed to the PSF of SINFONI or HST and resampled to the pixel size of SINFONI or HST. We also added noise at a level typical of our poorest data, to be conservative. In these images that match the SINFONI-HST resolution, the gas mass is estimated by using the pixel surface brightness method suggested by us (i.e., by adding the Σ_{gas} inferred by the Σ_{SFR} measured in each pixel). The resulting gas mass inferred for the AMAZE galaxies by using our method are reported in Table 4, Col. 2. We also applied the method adopted previously of inferring the average Σ_{gas} from the effective radius (Eq. (2)). In the latter case we have been optimistic, in the sense that we have bypassed the measurement of radius in the simulated images (which introduces additional

³ Some indications of evolution of the S-K at high- z were found by [Tacconi et al. \(2013\)](#) and [Santini et al. \(2014\)](#); however, as pointed out by [Santini et al. \(2014\)](#), the evolution, if any, is mild and galaxies at all redshifts can be fitted reasonably well with a single (integrated) S-K law with a slope of 1.5.

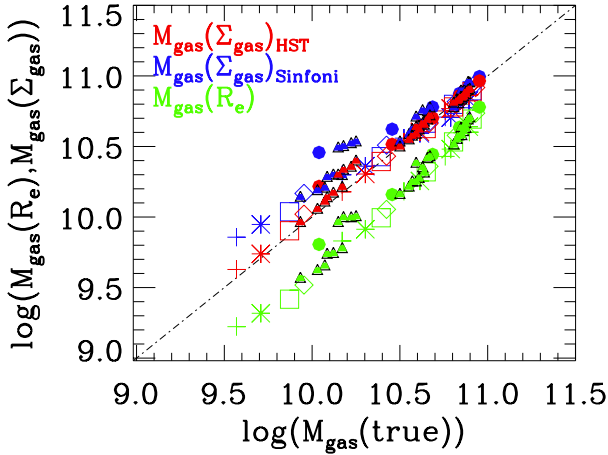


Fig. 7. Mass of gas of the simulated galaxies with different Sérsic profiles ($0.5 < n < 4$) and different effective radii ($5 < R_e < 2.5$ kpc) inferred with the two different methods discussed in the text. The x -axis shows the true gas mass (input in the simulated galaxy), while the y -axis shows either the gas mass calculated with the old method of using the total SFR and effective radius to infer an average gas surface density ($M_{\text{gas}}(R_e)$, green symbols), or the gas mass calculated with our new method, measuring the Σ_{gas} pixel by pixel in the data ($M_{\text{gas}}(\Sigma_{\text{gas}})$, red and blue symbols). Red symbols show the simulations of HST data and blue symbols show the simulation of SINFONI data. The green symbols are independent of the method since they use the integrated properties of galaxies. Galaxies modeled with Sérsic indices $n = 0.5, 1, 2, 3, 4$ are shown by crosses, asterisks, squares, diamonds, and circles, respectively. Interacting systems are marked with black triangles.

uncertainties) by directly taking the effective radius given in the simulation.

In Fig. 7, a comparison of these two methods is shown. The dash-dotted line indicate the 1:1 relation, where the measurements would recover exactly the true gas mass given in the simulation. Clearly, the old (R_e) method significantly underestimates the true gas mass by as much as a factor of three. Instead, our new method recovers the true gas mass with an accuracy better than 20% in most cases.

The resulting gas mass M_{gas} can be compared with the total baryonic mass $M_* + M_{\text{gas}}$ to estimate the gas mass fraction. The gas fraction $f_{\text{gas}} = M_{\text{gas}} / (M_{\text{gas}} + M_*)$ is an indicator of the galaxy evolutionary stage. Galaxies with a low gas fraction are systems that already used their gas to form stars and are becoming old (such as most local galaxies in Saintonge et al. 2011), while galaxies with a low gas fraction still have to convert the bulk of the available gas into stars. In Fig. 8, left panel, the resulting gas fractions are plotted as a function of the galaxy mass. The red symbols denote the AMAZE and LSD galaxies at $z \sim 3.4$ and at $z \sim 5$. For comparison, the yellow solid circles show the average gas fractions of local massive galaxies (with $M > 10^{10} M_{\odot}$) in bins of stellar mass, whose gas content has been measured by Saintonge et al. (2011) through direct CO observations. The green triangles and asterisks show the average gas fractions, also measured through direct CO observations, of galaxies at $z \sim 1$ – 2.73 in bins of stellar mass (Daddi et al. 2010; Tacconi et al. 2013; Saintonge et al. 2013).

There is an anticorrelation between gas content and galaxy stellar mass, which was previously noticed in samples observed directly in CO (Tacconi et al. 2013) at lower redshifts (and high stellar masses) and also observed by using the dust mass as a proxy of the gas mass at $0 < z < 2.5$ (Santini et al. 2014). However, part of this anticorrelation may be associated with bias

effects at low masses. Indeed, one should take into account that at low stellar masses our (indirect) method of deriving the gas mass is subject to incompleteness. Indeed, our sample is limited in SFR; since we estimate the gas mass through the Σ_{SFR} (by inverting the S-K law), our SFR limit indirectly translates into a lower limit on the gas mass that we can probe. Moreover, since $\Sigma_{\text{SFR}} \propto \text{SFR}/r^2$ and since the galaxy mass is known to correlate with galaxy radius ($M_* \propto r^{0.4}$), our lower limit on the gas content also indirectly depends on the galaxy mass. The solid lines in Fig. 8 show the inferred incompleteness limit for the AMAZE sample of unlensed galaxies (black line), which has a minimum SFR of $5 M_{\odot} \text{ yr}^{-1}$, and for the lensed galaxies in the AMAZE sample (red line), which have a minimum SFR of $1 M_{\odot} \text{ yr}^{-1}$. The lack of AMAZE and LSD galaxies below these lines is probably not intrinsic to the distribution of galaxies at $z \sim 3$, but is possibly due to incompleteness. However, we note that the location of the four lensed galaxies in AMAZE is significantly above the incompleteness line, and they still show a clear drop of gas fraction as a function of stellar mass. Therefore, the anticorrelation between gas fraction and stellar mass may indeed be real, and would be in line with the findings of direct CO observations at lower redshifts (Tacconi et al. 2013), although at higher stellar masses and lower redshifts. This result would support the downsizing scenarios, where massive galaxies at $z \sim 3$ have already consumed or ejected a significant fraction of gas, while low-mass galaxies are evolving more slowly.

The right panel of Fig. 8 shows the gas fraction as a function of $s\text{SFR} = \text{SFR}/M_{\text{star}}$, which is a tracer of the evolutionary stage of galaxies. As recently found by Tacconi et al. (2013) at lower redshifts, there is a correlation between gas fraction and $s\text{SFR}$, suggesting that more evolved galaxies (lower $s\text{SFR}$) have lower gas fraction, because gas has been consumed by star formation (and expelled by the supernovae activity). However, in this case as well, our results are affected by incompleteness at low $s\text{SFR}$ as a consequence of the SFR limit of our sample.

Either samples extending to lower SFR or direct measurements of the gas content (e.g., through CO mm observations) at $z > 3$ are required to validate these trends and verify that they are not a consequence of selection effects.

At masses higher than $10^{10} M_{\odot}$ the incompleteness of our sample, in terms of gas fraction, is very low. Hence our data at $M_* > 10^{10} M_{\odot}$ can be used, along with results at lower redshift, to constrain the evolution of the gas fraction in galaxies out to $z \sim 3.4$.

The left panel of Fig. 9 shows the evolution of the gas fraction in galaxies divided into different bins of stellar mass (to minimize the variation effect of the gas fraction with stellar mass, which is found to occur also at these high masses Santini et al. 2014). Although with high dispersion, the average gas fraction in massive galaxies shows a rapid increase by over an order of magnitude from $z = 0$ to $z \sim 2$, which was previously reported (Tacconi et al. 2010, 2013; Daddi et al. 2010). At higher redshift our data show that the evolution of the gas fraction flattens, and there is a mild indication that it may even begin to decrease. This finding is in line with the result by Magdis et al. (2012a), who found indications for a flattening of the evolution of the gas fraction in galaxies at $z \sim 3$ based on CO observations of two galaxies (one of which is an upper limit). The evolution of the gas fraction in massive galaxies strongly resembles the evolution of the cosmic density of the SFR (Hopkins & Beacom 2006) and provides additional support to the scenario in which the cosmic evolution of the SFR in galaxies is driven by the evolution of their molecular content, as suggested by Obreschko & Rawlings (2009).

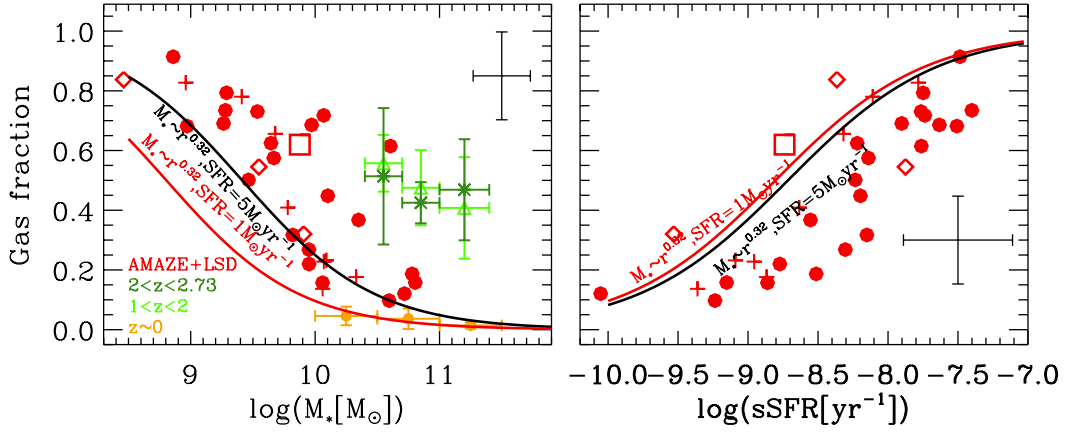


Fig. 8. Gas fraction as a function of stellar mass and sSFR. The red symbols show the AMAZE+LSD galaxies at $z \sim 3-5$ (same symbol-coding as Fig. 2). The solid lines show the incompleteness limit in the AMAZE unlensed (black) and lensed (red) galaxies. In the *left panel* the orange dots show the average gas fractions of local massive galaxies in bins of stellar mass, while green asterisks and triangles show the averages of the galaxies at $1 < z < 2$ and $2 < z < 2.73$, respectively, whose gas content has been measured through CO observations (Daddi et al. 2010; Saintonge et al. 2011, 2013; Tacconi et al. 2013). The upper-right error bars show the median error on the gas fraction and on the stellar mass in our sample. *Right panel:* gas fraction as a function of the sSFR, with the same symbol code as in the *left panel*.

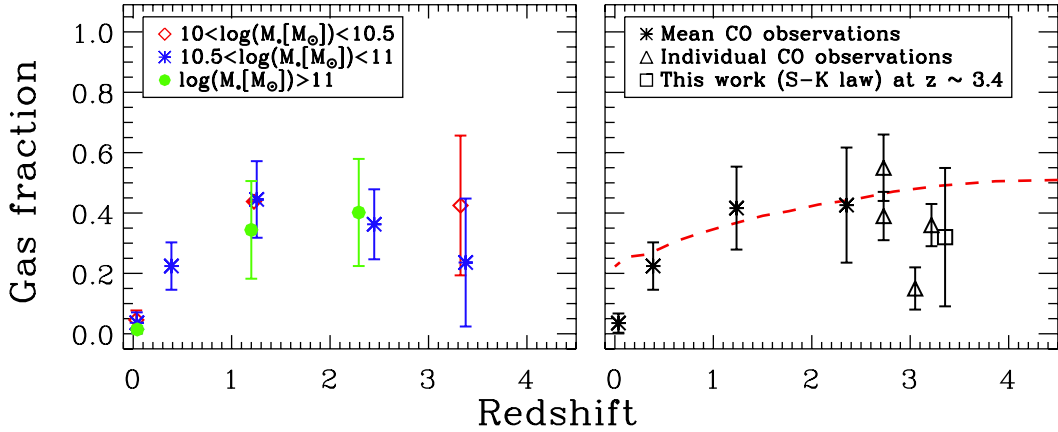


Fig. 9. Gas fraction as a function of redshift from a compilation of measurements in the redshift range $0 \leq z \leq 3.7$ (same data of Fig. 8) and including our new results. *Left panel:* results averaged in bins of stellar mass. *Right panel:* black asterisks show the average (over the whole mass range at $M_* > 10^{10} M_\odot$) evolution of the gas fraction up to $z \sim 3.4$. At $z \geq 2.7$, the triangles show the individual values inferred from direct CO observations (Riechers et al. 2010; Magdis et al. 2012a; Saintonge et al. 2013). The hollow square is the average measurement at $z \sim 3.4$ determined in this work by inverting the S-K law. The dashed red line shows the evolution of the gas fraction from the semianalytic models of Lagos et al. (2011).

The right panel of Fig. 9 shows the inferred evolution of the gas fraction in galaxies, where we took the average in different redshift bins from the left panel. While the asterisks show the direct CO measurements (averages at $z < 3$ and individual detections at $z > 3$), the hollow square indicates the average of our measurements at $z \sim 3.4$, obtained by inverting the S-K law. The prediction of the cosmological models obtained by Lagos et al. (2011) is indicated with a red dashed line, which shows the expected average for the total population of star-forming galaxies with vigorous SFR ($> 10 M_\odot \text{ yr}^{-1}$), that is, a range similar to our sample. The models described by Lagos et al. (2011) do indeed associate the evolution of the SFR with the evolution of the content of molecular gas in galaxies. The model expectations for strongly star-forming galaxies is consistent, within the dispersion and error bars (although on the high side), with the observed evolution of the gas fraction in massive galaxies.

7. Comparison with simple models

Several models have been proposed to explain the metallicity evolution in galaxies. Here we attempt a very simple modeling

to constrain the inflow and outflow in galaxies at $z > 3$. Key quantities for investigating these questions are the metallicity, the gas fraction, and the effective yield, that is, the amount of metals produced and retained in the ISM per unit mass of formed stars. The latter quantity deserves a few introductory words.

In a closed-box model the metallicity is directly related to the gas fraction by the equation

$$Z = y \ln(1/f_{\text{gas}}), \quad (4)$$

where y is the true stellar yield, that is, the ratio between the amount of metals produced and returned into the ISM and the mass of stars. Nevertheless, during their lifetime, galaxies experience outflows (supernovae explosions, winds), inflows (pristine or enriched gas) and merging events. Therefore, the resulting metallicity generally differs from Eq. (4). One can invert Eq. (4) by defining the effective yield as

$$y_{\text{eff}} = Z / \ln(1/f_{\text{gas}}). \quad (5)$$

The effective yield is equal to the true yield for a galaxy that evolves like a closed box, while it may differ substantially in the

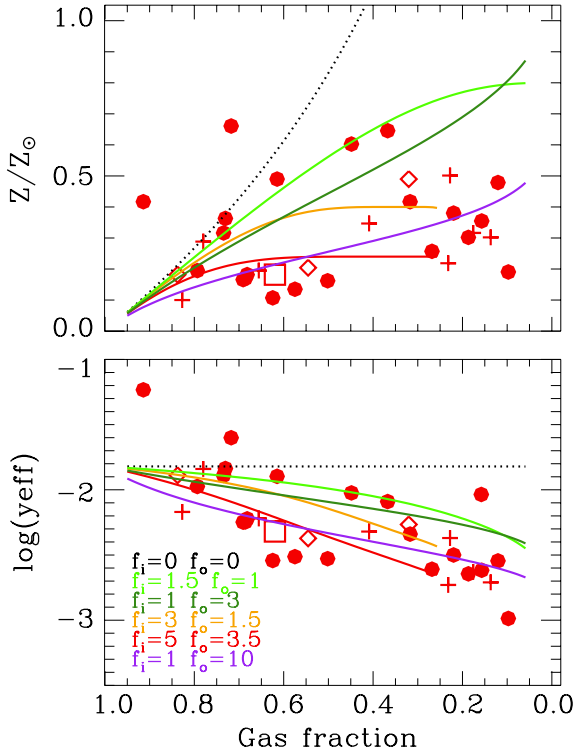


Fig. 10. Metallicities and effective yields as a function of gas fraction for the galaxies in our sample at $z \sim 3$, with the same symbols as in the previous figures. In both panels the Erb (2008) models for various inflows f_i , outflows f_o rates (relative to the SFR) are shown. The dotted black line is the closed-box model ($f_i = f_o = 0$). In the bottom panel (lower-right corner), the inflows and outflows rates in units of the SFR are shown for every model (with different color-coding).

case of metal enriched outflows and in the case of inflows of metal-poor gas. The effective yields computed for the AMAZE and LSD galaxies are given in Table 4.

To constrain inflow and outflow properties of $z > 3$ galaxies, we compared our results with the simple model described in Erb (2008). This model considers pristine gas accretion at a rate that is a constant fraction f_i of the SFR (i.e., as a continuous process or average of many minor events) and also an outflow rate f_o (of gas with the same metallicity as the current galaxy average) at a constant fraction of the SFR (i.e., the so-called mass-loading factor of the outflow).

In Fig. 10, the metallicity and effective yields are plotted as a function of the gas fraction. Red symbols show the metallicity and effective yields for the AMAZE and LSD galaxies.

For comparison, the bulk of the local disk galaxies (e.g., those in the SDSS sample), especially those with $M > 10^{10} M_\odot$, have a low gas fraction (< 0.2), metallicities around solar, and high effective yields, while massive galaxies at $z > 3$ with similar gas fractions have much lower metallicities and much lower effective yields.

The Erb (2008) models are overplotted with various inflow and outflow rates. The dotted black line is the closed-box model (i.e., $f_i = f_o = 0$), which falls far short of reproducing the bulk behavior of the AMAZE and LSD galaxies. The most suitable models for the bulk of the sample are those with both massive inflow rates $f_i = 1 - 5 \times SFR$ and massive outflow rates $f_o = 1.5 - 3.5 \times SFR$.

Massive cool inflows are indeed expected in the early Universe according to recent cosmological models (e.g. Dekel et al. 2009; van de Voort et al. 2012, and references therein),

although direct observational evidence is still scarce. In particular, no direct measurement of the inflow rate is available that could be compared with the high values inferred by us in this paper. Outflows are ubiquitously observed, both locally and at high redshift. However, in high- z star-forming galaxies the typical load factor (f_o) measured in observations is generally about one or a few (Steidel et al. 2010; Genzel et al. 2011; Newman et al. 2012). Our data require a load factor of at least a few, and even $f_o \geq 3$ for the most extreme galaxies at $z > 3$.

Achieving such a high outflow rate in models of star-forming galaxies is difficult. However, a possibility is that this high outflow rate might be associated with AGN/quasar activity. Very high quasar-driven outflow rates have been observed both locally (Feruglio et al. 2010; Sturm et al. 2011; Rupke & Veilleux et al. 2011; Ciccone et al. 2012) and at high redshift (Cano-diaz et al. 2012; Maiolino et al. 2012). Although the galaxies in the AMAZE sample show no evidence for AGN activity, black-hole feedback may have occurred in cyclic episodes and driven enriched gas out of the galaxy. Such massive inflows and outflows may be responsible for bringing the early galaxies out of the equilibrium that characterizes galaxies at lower redshifts and causes them to deviate from the FMR.

8. Metallicity gradients at $z \sim 3$

As mentioned in the introduction, metallicity gradients provide important information on the formation mechanism of galaxies. Mapping the gas metallicity in high- z galaxies is extremely challenging, because the surface brightness of the emission lines in galaxies is low and the emission is often unresolved in seeing-limited images. Cresci et al. (2010) presented the first metallicity maps at $z > 3$ by exploiting data of three bright and resolved AMAZE galaxies, out of the first subsample observed initially (Maiolino et al. 2008). Here we present resolved metallicity maps for a total of eleven galaxies in the AMAZE sample, for which the S/N of each spectral-pixel and the spatial extension allow us to extract information on their spatially resolved metal content.

In the same way as for the integrated metallicities, the metallicity maps were determined by means of a combination of strong line-diagnostics based on $H\beta$ and $[OIII]\lambda 5007$ shifted into the K band, and $[OII]\lambda 3727$ shifted into the H band for sources at $3 < z < 3.7$, as mentioned at the beginning of Sect. 5 and as detailed in Appendix B. The derived metallicity maps and flux maps are shown in Figs. 11–13. In the same figures we also show the $[OIII]/[OII]$ line ratio, which is a proxy of the ionization parameter, but which also correlates with the metallicity, although with a high dispersion, which is useful to remove the degeneracy in the R_{23} parameter. Regions with an error on the metallicity larger than about 0.15–0.2 dex are masked out (for strongly asymmetric error bars the points were retained when the shortest error bar provided evidence of a clear metallicity variation with respect to other points in the galaxy). The black cross in each map indicates the peak of the continuum flux. As found by Cresci et al. (2010) for the initial subsample of three galaxies, the peak of the star formation activity, as traced by $H\beta$ and $[OIII]\lambda 5007$ emission, is spatially correlated with the region of the galaxy with the lowest metallicity. A clear exception is CDFS4414 where the metallicity tends to be flat.

To increase the S/N on the outer region we also obtained the radial metallicity variation by integrating the line fluxes within a central aperture (a few kpc in radius) and in an outer ring (with an outer radius typically extending to about 8–10 kpc). The resulting metallicity radial profiles are shown in Figs. 14 and 15.

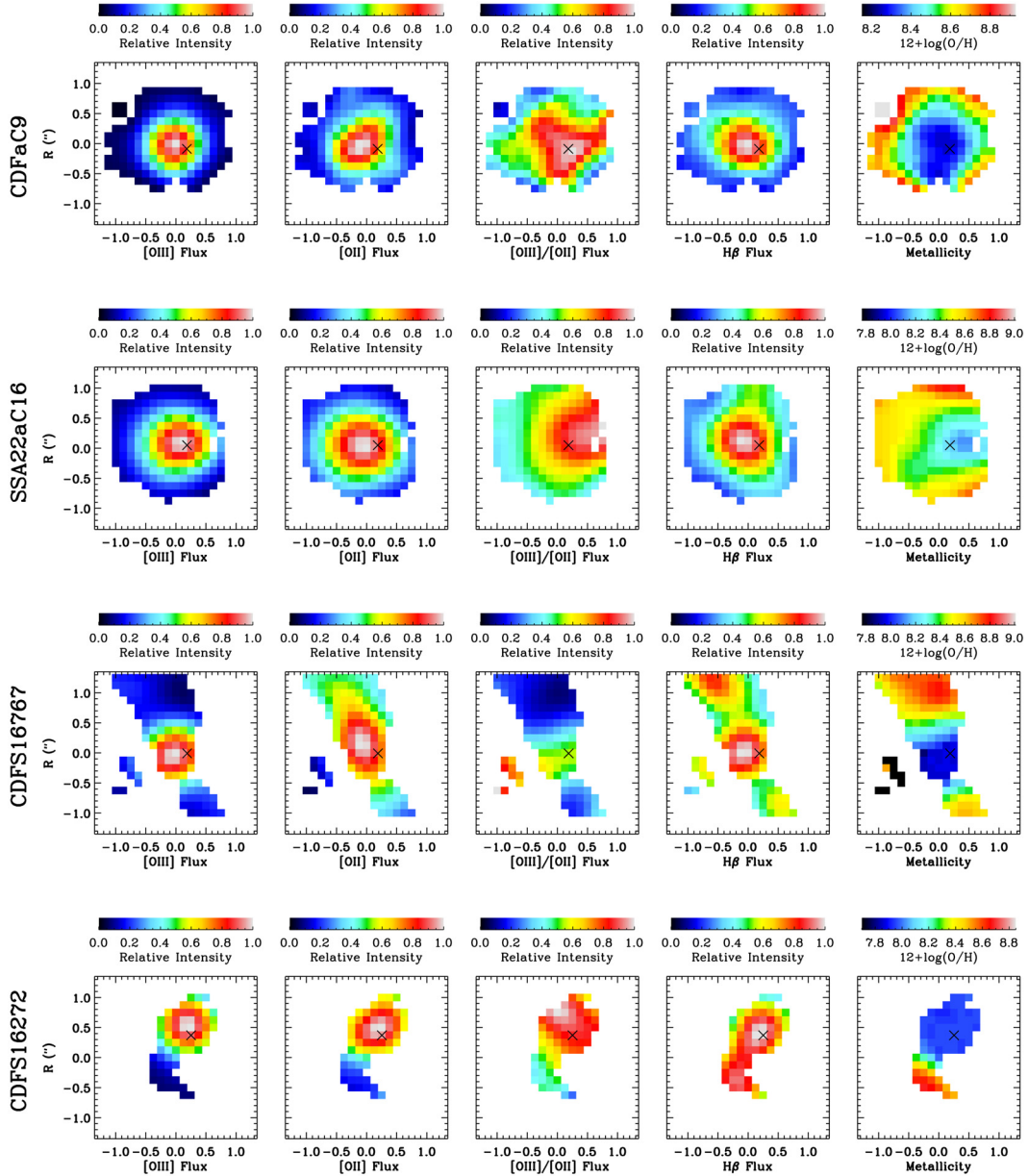


Fig. 11. [OIII]5007, [OII]3727, H β flux maps, [OIII]5007/[OII]3727 ratio, and metallicity maps for the galaxies CDFaC9, SSA22aC16, CDFS11991, and CDFS16272.

For DFS2237bC21 it was not possible to determine the metallicity of the outer region because of the low S/N even in the spectrum integrated in the annulus. The resulting radial metallicity gradients are reported in Table 5. Most of the gradients are flat or inverted (positive).

For the flat gradients one should keep in mind that as pointed out by Yuan et al. (2013), these shallow gradients may be partially due to the low angular resolution. However, we also note that the two-dimensional metallicity maps show complex, nonradially symmetric patterns, which were averaged out when we obtained averages in radial annuli. We found no significant dependence of the metallicity gradients as a function of stellar mass, SFR, and sSFR.

We also investigated the metallicity gradients as a function of morphology and the dynamical status. Figure 14 gathers all galaxies that according to the HST images are isolated, while Fig. 15 include all galaxies that are in close interaction (a companion within 30 kpc) or with strongly irregular morphology

(in the H band), presumably associated with late mergers. There is no relation between the morphological properties (isolated versus interacting) and the trend of the metallicity gradient. The dynamical status (rotating disk versus non-rotating), as inferred by Gnerucci et al. (2011a), is also reported in each panel, when available. It is interesting to note that most of the systems with inverted gradients are associated with rotating disks, as was suggested by Cresci et al. (2010) for the first subsample of three galaxies. At least at $z > 3$, these results do not fully support the scenario in which inverted gradients are preferentially associated with galaxy interactions/mergers that according to some models (e.g. Rupke et al. 2010; Perez et al. 2011; Pilkington et al. 2012; Torrey et al. 2012) are supposed to drive pristine gas from the outskirts to the inner region. Instead, smooth inflows of pristine gas toward the central region, both diluting the gas metallicity and enhancing star formation, may be responsible for the gradients observed at $z > 3$. The chemical evolutionary model described by Mott et al. (2013) do indeed fit our oxygen abundance

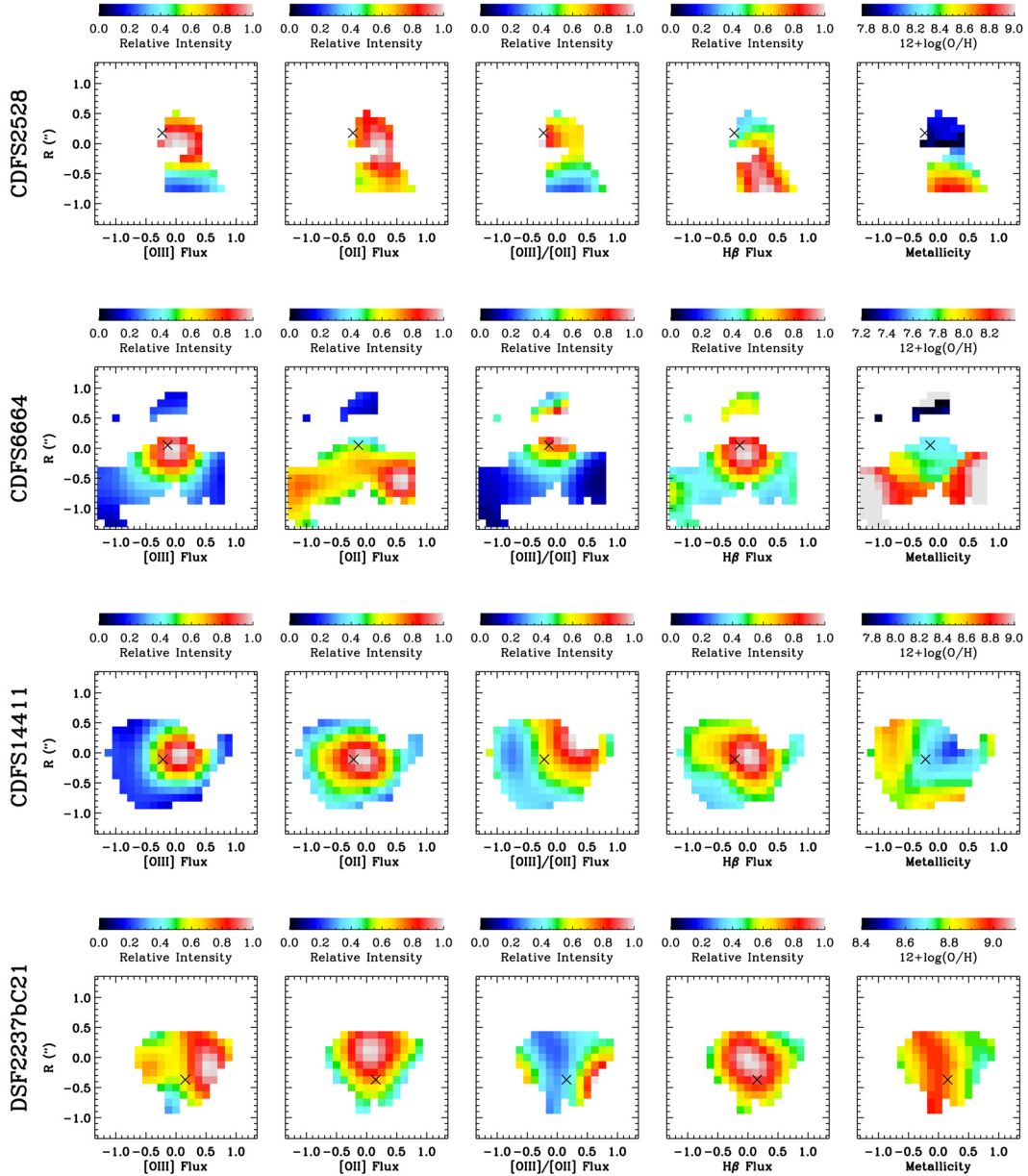


Fig. 12. [OIII]5007, [OII]3727, $H\beta$ flux maps, [OIII]5007/[OII]3727 ratio, and metallicity maps for the galaxies CDFS2528, CDFS6664, CDFS14411, and DSF2237bC21.

gradients at $z \sim 3$ and also reproduce the oxygen and iron gradients of the Milky Way when an inside-out formation of the disk, a constant star formation efficiency, and time-dependent velocity radial flows are assumed.

Nevertheless, it is clear from Figs. 11 to 13 that the metallicity gradients are generally not radially symmetric, hence the radial averages shown obtained in Figs. 14, 15 and in Table 5 can be deceiving, and moreover, tend to dilute more pronounced gradients observed in the metallicity maps of galaxies.

To avoid the radial-average approach, and to investigate in more detail the scenario in which lower metallicity regions are associated with star-forming regions by an excess of (pristine) gas that both dilutes metallicity and boosts star formation, we compared the spatially resolved metallicity with the surface gas density (obtained by inverting the S-K law). This comparison is shown for each galaxy in Figs. 16 and 17, where each point shows the metallicity and Σ_{gas} at each pixel. We verified that the correlated errors on the two axes (because the $H\beta$ flux was used

on both axes) does not introduce a significant artificial correlation. Moreover, not all of the plotted points are fully independent of each other because of the seeing. However, in most galaxies there is a clear anticorrelation between metallicity and Σ_{gas} , which additionally supports the inflow/dilution scenario.

However, Σ_{gas} is not necessarily illustrative of the evolutionary stage of individual regions of each galaxy. The gas fraction is more useful to constrain the local evolutionary processes. But it is difficult to obtain resolved information on the gas fraction, since it is not easy to determine the stellar mass surface density. Yet, for a few galaxies for which we resolved the distribution of the nebular lines (for which we hence have spatially resolved information on Σ_{gas} by inverting the S-K relation) we also have deep HST-WFC3 images in the H band, sampling the V -band rest frame. To a first approximation, we can assume that the Σ_{star} scales proportionally to the rest-frame V -band surface brightness (the normalization factor is given by the constraint that the total V -band light should be associated with the total

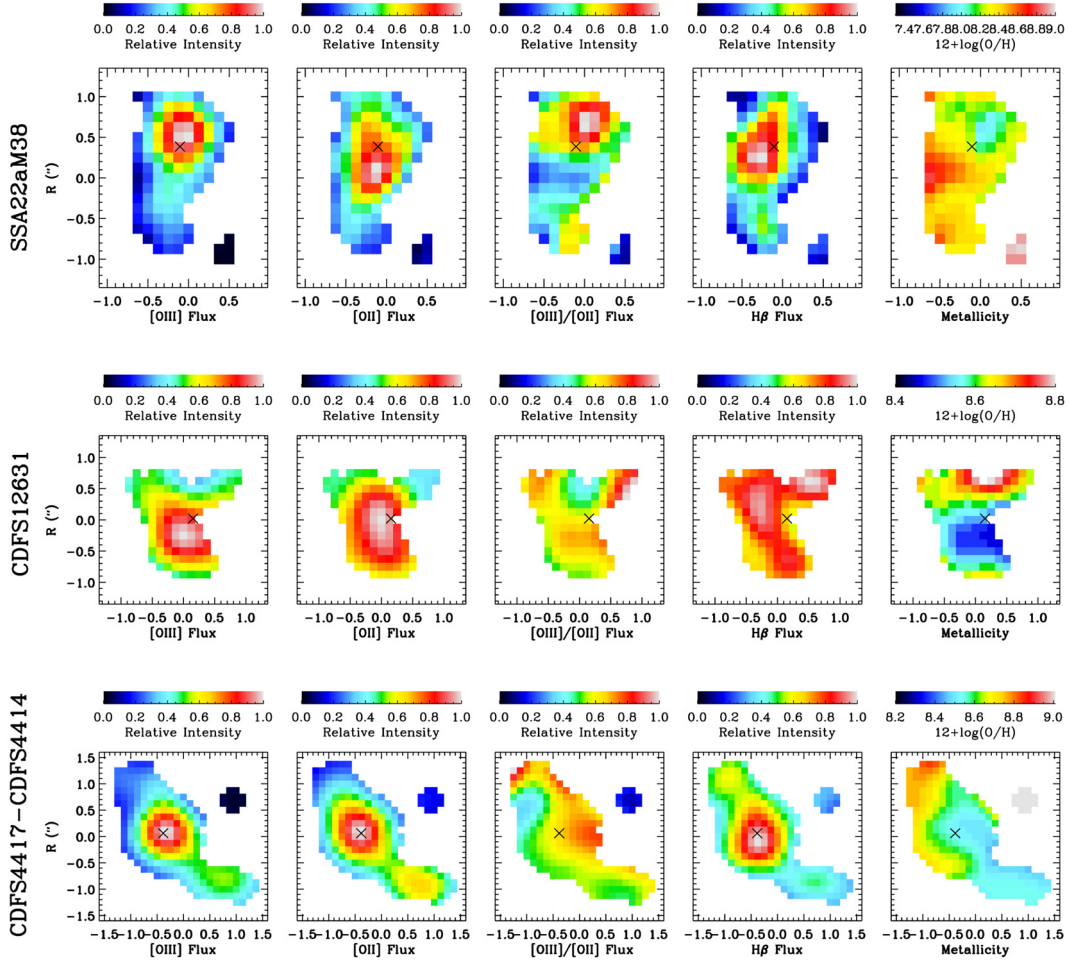


Fig. 13. [OIII]5007, [OII]3727, H β flux maps, [OIII]5007/[OII]3727 ratio, and metallicity maps for the galaxies SSA22aM38, CDFS12631, and the interacting galaxies CDFS4417–CDFS4414.

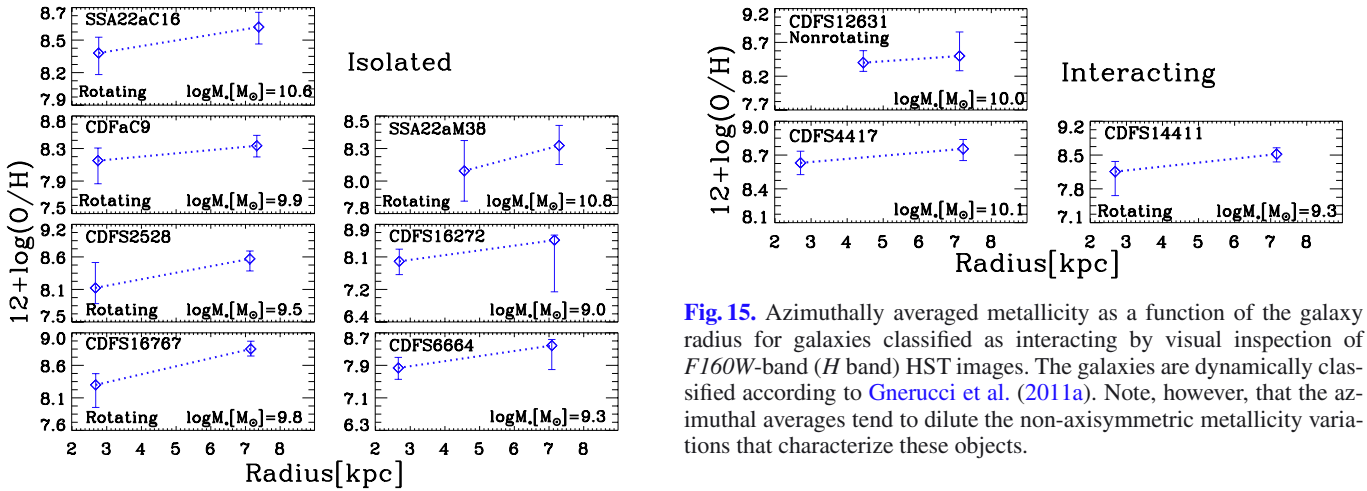


Fig. 14. Azimuthally averaged metallicity as a function of the galaxy radius for galaxies classified as isolated by visual inspection of $F160W$ -band (H band) HST images. The galaxies are dynamically classified according to Gnerucci et al. (2011a). Note, however, that the azimuthal averages tend to dilute the non-axisymmetric metallicity variations that characterize these objects.

stellar mass inferred by the detailed multiband SED modeling). We could therefore estimate the gas fraction in the same inner and outer regions for which the metallicity could be inferred.

Fig. 15. Azimuthally averaged metallicity as a function of the galaxy radius for galaxies classified as interacting by visual inspection of $F160W$ -band (H band) HST images. The galaxies are dynamically classified according to Gnerucci et al. (2011a). Note, however, that the azimuthal averages tend to dilute the non-axisymmetric metallicity variations that characterize these objects.

Figure 18 shows the metallicity as a function of the gas fraction for the four galaxies for which we can resolve both the metallicity and the gas fraction. Blue symbols indicate the inner regions, while red symbols indicate the outer regions. In all these galaxies the inner region has a lower metallicity and higher gas fraction than the outer region. This finding is in line with the result of Cresci et al. (2010), suggesting that the inner regions suffer from metallicity dilution from inflow of pristine gas, which centrally both increases the gas fraction and dilutes the metallicity.

Table 5. Metallicity differences between inner and outer galaxy regions inferred from the near-IR spectra.

Name	$12 + \log(\text{O}/\text{H})_{\text{inner}}$	$12 + \log(\text{O}/\text{H})_{\text{outer}}$	$\Delta 12 + \log(\text{O}/\text{H})$
CDFaC9	$8.18^{+0.17}_{-0.31}$	$8.38^{+0.14}_{-0.15}$	$0.20^{+0.22}_{-0.34}$
CDFS4417	$8.60^{+0.10}_{-0.10}$	$8.72^{+0.08}_{-0.10}$	$0.12^{+0.13}_{-0.14}$
CDFS6664	$7.83^{+0.26}_{-0.28}$	$8.38^{+0.15}_{-0.59}$	$0.55^{+0.30}_{-0.65}$
CDFS16767	$8.28^{+0.16}_{-0.32}$	$8.79^{+0.11}_{-0.10}$	$0.51^{+0.19}_{-0.34}$
CDFS2528	$8.10^{+0.42}_{-0.26}$	$8.58^{+0.13}_{-0.20}$	$0.48^{+0.44}_{-0.33}$
CDFS16272	$7.95^{+0.31}_{-0.34}$	$8.49^{+0.13}_{-1.32}$	$0.54^{+0.34}_{-1.36}$
CDFS12631	$8.41^{+0.18}_{-0.13}$	$8.51^{+0.36}_{-0.22}$	$0.10^{+0.40}_{-0.26}$
CDFS14411	$8.13^{+0.21}_{-0.49}$	$8.49^{+0.25}_{-0.16}$	$0.36^{+0.25}_{-0.52}$
SSA22aM38	$8.10^{+0.24}_{-0.24}$	$8.30^{+0.16}_{-0.15}$	$0.20^{+0.29}_{-0.28}$
SSA22aC16	$8.34^{+0.14}_{-0.19}$	$8.57^{+0.13}_{-0.15}$	$0.23^{+0.19}_{-0.24}$
Composite ^a	$8.13^{+0.23}_{-0.18}$	$8.56^{+0.44}_{-0.29}$	$0.43^{+0.50}_{-0.34}$

Notes. Column 1, object name; Col. 2, gas metallicity of the inner aperture within a radius of $0.375''$; Col. 3, gas metallicity of the outer region within a radius of $0.375'' < r < 1''$; Col. 4, metallicity difference between inner and outer regions. ^(a) The same values as described above are reported for the composite spectra of the ten galaxies presented in this table.

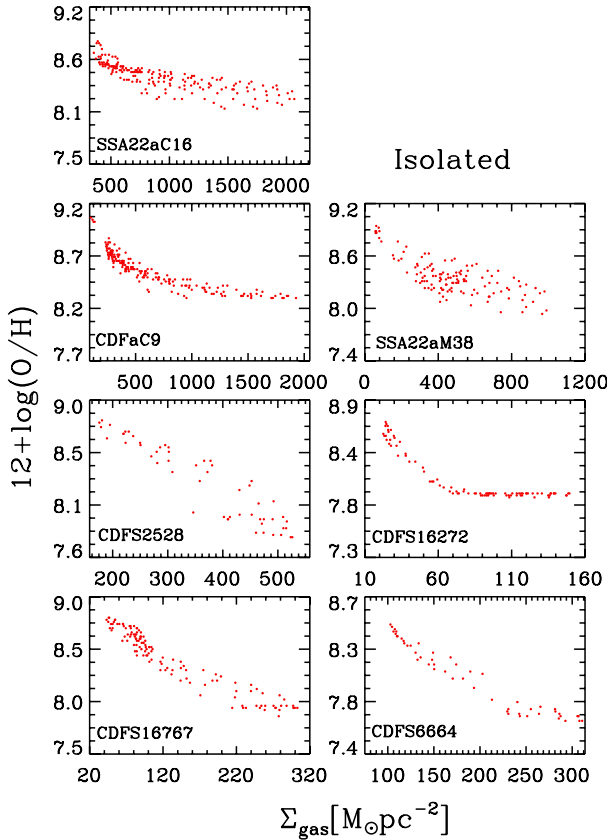


Fig. 16. Spatially resolved metallicities as a function of the gas surface density of isolated galaxies.

However, we note that several points, especially those in the outer regions, have higher metallicities than those of the closed-box model. This may indicate that our metallicity calibration is biased high or, alternatively, that in these regions the stellar yields are higher than the average of a normal stellar population (e.g., through recent injection of metals by massive stars, which

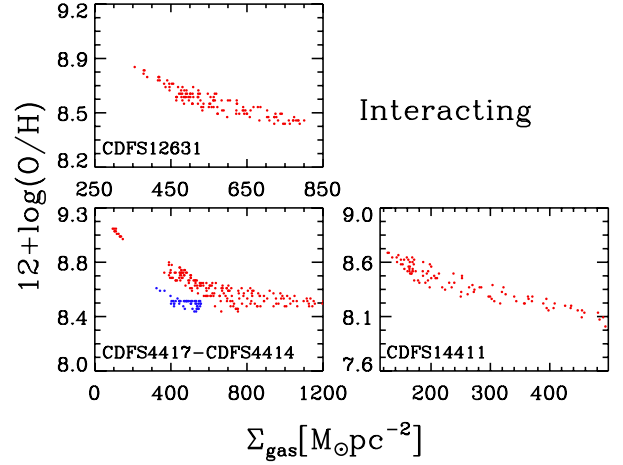


Fig. 17. Spatially resolved metallicities as a function of the gas surface density of interacting galaxies. Blue dots show the distribution of the galaxy CDFS4414 that interacts with CDFS4417.

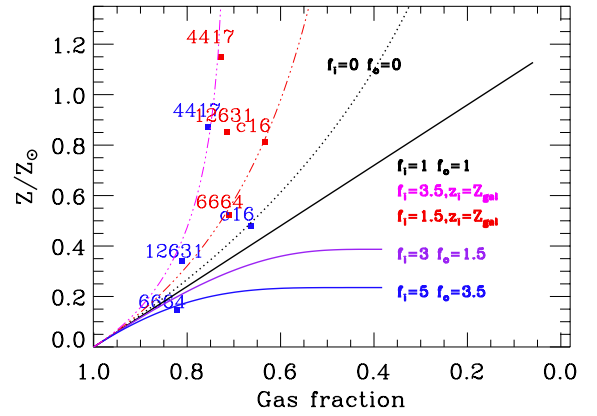


Fig. 18. Metallicity as a function of the gas fraction for the inner/outer galaxy regions. Blue squares show the inner regions, while red squares show the outer regions. Blue and purple solid lines show models with outflows and inflows of pristine gas. The dotted black line shows the closed-box model. Dash-dotted red and magenta lines show models with enriched inflows (with the same metallicity as the galaxy) and no outflows.

have higher yields than average). An additional, alternative explanation for the high metallicity in these regions, especially in the outer ones, is inflow of metal-enriched gas, which can give a higher metal content than expected from the closed-box model. Indeed, in several recent models of galactic fountains, a significant fraction of the metals ejected from the central winds falls back onto the outer parts of the galaxy.

We explored the latter scenario by using the model of Erb (2008). We constructed additional models in which the gas inflow is not pristine, but has a metallicity equal to the metallicity of the bulk of the galaxy. These models are shown with red and magenta lines in Fig. 18 and nicely reproduce the observed values in the outer regions of several of these galaxies. Therefore, enhanced metallicity transport from the inner to the outer regions through galactic fountains may be an additional mechanism responsible for the inverted gradients in these young systems.

9. Conclusions

We have reported the results of a program aimed at measuring optical nebular emission lines in a sample of 35 star-forming

galaxies at $z \sim 3.4$ by using SINFONI, the near-infrared integral field spectrograph at the VLT. The integrated and spatially resolved spectral information allowed us to constrain the metallicity and, indirectly, the amount of gas hosted in these galaxies. The main results are summarized as follows:

- On average the galaxies in our sample at $z \sim 3.4$ are metal poorer, by $-0.43^{+0.16}_{-0.18}$ dex, than the fundamental relation between metallicity, stellar mass, and SFR (FMR) that characterizes local and lower-redshift galaxies ($0 < z < 2.5$). Galaxies at $z \sim 3.4$ have a metallicity dispersion of about 0.25 dex in the FMR, much higher than local galaxies (which have $\sigma \sim 0.05$), which probably reflects a mixture of different stages of unsteady chemical evolutionary processes at this epoch, in contrast to what is observed at later epochs.
- There is no significant correlation between the dynamical state of these galaxies and the deviations from the FMR. More specifically, galaxies characterized by regular rotation patterns have, on average, the same metallicity deviations from the FMR as galaxies with irregular kinematics (indicative of recent/ongoing merging). These results suggest that the enhanced merging rate at $z > 3$ is unlikely to be the main reason for the deviations from the FMR at $z > 3$.
- We found that the deviations from the FMR at $z \sim 3.4$ correlate with $\mu_{32} = \log(M_*) - 0.32 \log(SFR)$, which is the parameter giving the projection of the FMR that minimizes the dispersion, and which is associated with the star formation efficiency as well as with the presence of outflows and inflows.
- By mapping the optical nebular emission lines and by inverting the Schmidt-Kennicutt relation, we inferred the amount of molecular gas hosted in these galaxies. At $z \sim 3$, the average gas fraction of massive galaxies ($M_* > 10^{10} M_\odot$) does not follow the steep increasing evolution observed from $z = 0$ to $z \sim 2$. Between $z \sim 2$ and $z \sim 3$ the average gas fraction in galaxies remains constant or possibly even decreases. Our results support the scenario in which the evolution of cosmic star formation in galaxies is primarily driven by the evolution of the amount of gas in galaxies, and not by an evolution in the efficiency of star formation.
- The observed anticorrelation between gas fraction and stellar mass, as well as the correlation between gas fraction and sSFR, may support the scenario in which downsizing is in place at $z \sim 3$. However, new observations are required to verify this trend and validate that it is not a consequence of selection effects.
- Models with both high inflows and outflows rates ($\sim 2\text{--}5 \times SFR$) are necessary to reproduce the measured galaxy properties, and in particular the metallicities, gas fraction, and effective yields. These massive flows in the early Universe are most likely responsible for the different properties and deviations of galaxies at $z \sim 3$ compared with local and lower redshift galaxies.
- By mapping the distribution of the star formation and metallicity in 10 out of 34 galaxies at $z \sim 3$, we found an spatial anticorrelation between the peak of the SFR and the lowest metallicity region. We furthermore found within each galaxy an anticorrelation of metallicity and gas surface density. This result supports the models in which smooth gas inflows feed galaxies at high redshift. In this scenario the pristine infall both boosts star formation (through the Schmidt-Kennicutt law) and dilutes the metallicity, generating the observed anticorrelation.

- For four AMAZE galaxies, it was possible to determine the metallicity and gas fraction in the inner ($r < 3$ kpc) and in the out outer ($3 < r < 8$ kpc) galaxy regions. In all these galaxies, the inner region has a lower metallicity and higher gas fraction than the outer region. This finding suggests that the inner regions suffer from metallicity dilution from inflows of pristine gas, which centrally increases the gas fraction and dilutes the metallicity. However, nuclear enriched outflows probably contribute to lower the metallicity in the central region. Additional modeling supported the galactic-fountain scenario in which outflows of enriched material are expelled from the inner region and fall back, as inflows of enriched material, onto the galaxy outskirts.

Acknowledgements. This work was funded by the Marie Curie Initial Training Network ELIXIR 214227 of the European Commission. We also acknowledge partial support by INAF. Alessandro Marconi acknowledges support from grant PRIN-MIUR 2010-2011 “The dark Universe and the cosmic evolution of baryons: from current surveys to Euclid”.

References

- Andrews, B. H., & Martini, P. 2013, *ApJ*, 765, 140
- Arrigoni, M., Trager, S. C., Somerville, R. S., & Gibson, B. 2010, *MNRAS*, 402, 173
- Baffa, C., Comoretto, G., Gennari, S., Lisi, F., et al. 2001, *A&A*, 378, 722
- Belli, S., Jones, T., Ellis, R., & Richard, J. 2013, *ApJ*, 772, 141
- Bigiel, P., Leroy, A., Walter, F., et al. 2008, *AJ*, 136, 2846
- Bongiovanni, A., Oteo, I., Cepa, J., et al. 2010, *A&A*, 519, L4
- Bouché, N., Cresci, G., Davies, R., et al. 2007, *ApJ*, 671, 303
- Bouché, N., Dekel, A., Genzel, R., et al. 2010, *ApJ*, 718, 1001
- Bothwell, M. S., Maiolino, R., Kennicutt, R., et al. 2013, *MNRAS*, 433, 1425
- Brooks, A. M., Governato, F., Booth, C. M., et al. 2007, *ApJ*, 655, L17
- Bruzual, G., & Charlot, S. 2003, *MNRAS*, 344, 1000 (BC03)
- Calura, F., & Menci, N., 2009, *MNRAS*, 400, 1347
- Calzetti, D., Armus, L., Bohlin, R. C., et al. 2000, *ApJ*, 533, 682
- Cano-Diaz, M., Maiolino, R., Marconi, A., et al. 2012, *A&A*, 537, L8
- Castellano, M., Sommariva, V., Fontana, A., et al., 2013, *A&A*, submitted
- Cescutti, G., Matteucci, F., François, P., & Chiappini, C. 2007, *A&A*, 462, 943
- Cicone, C., Feruglio, C., & Maiolino, R., et al. 2012, *A&A*, 543, A99
- Cresci, G., Mannucci, F., Maiolino, R., et al. 2010, *Nature*, 467, 811
- Cresci, G., Mannucci, F., Sommariva, V., et al. 2012, *MNRAS*, 421, 262
- Conselice, C. J., Mortlock, A., Bluck, A. F. L., et al. 2013 *MNRAS*, 430, 1051
- Coppin, K. E. K., Swinbank, A. M., Neri, R., et al. 2007, *AJ*, 665, 936
- Daddi, E., Bournaud, F., Walter, F., et al. 2010, *ApJ*, 713, 686
- Davé, R., Finlator, K., & Oppenheimer, B. D. 2011, *MNRAS*, 416, 1354
- Davé, R., Finlator, K., & Oppenheimer, B. D. 2012, *MNRAS*, 421, 98
- Dayal, P., Ferrara, A., & Dunlop, J. S. 2013, *MNRAS*, 430, 2891
- de Rossi, M. E., Tissera, P. B., & Scannapieco, C. 2007, *MNRAS*, 374, 323
- Dekel, A., Birnboim, Y., Engel, G., et al. 2009, *Nature*, 457, 451
- Dickinson, M., Papovich, C., Ferguson, H. C. et al. 2003, *ApJ*, 587, 25
- Drory, N., Bender, R., Feulner, G., et al. 2004, *ApJ*, 608, 742
- Eisenhauer, F., Abuter, R., Bickert, K., et al. 2003, *Proc. SPIE*, 4841, 1548
- Ellison, S. L., Patton, D. R., Simard, L., & McConnachie, A. W. 2008, *ApJ*, 672, L107
- Erb, D. K. 2008, *ApJ*, 674, 151
- Erb, D. K., Steidel, C. C., Shapley, A. E., et al. 2006, *ApJ*, 646, 107
- Feruglio, C., Maiolino, R., Piconcelli, E., et al. 2010, *A&A*, 518, L155
- Finlator, K., & Davé, R. 2008, *MNRAS*, 385, 2181
- Forbes, J. C., Krumholz, M. R., Burkert, A., & Dekel, A. 2013, *MNRAS*, submitted [[arXiv:1311.1509](https://arxiv.org/abs/1311.1509)]
- Fynbo, J. P. U., Krogager, J.-K., Venemans, B., et al. 2013, *ApJS*, 204, 6
- Genel, S., Genzel, R., Bouché, N., et al. 2008, *ApJ*, 688, 789
- Genzel, R., Tacconi, L. J., Eisenhauer, F., et al. 2006, *Nature*, 442, 786
- Genzel, R., Tacconi, L. J., Gracia-Carpio, J., et al. 2010, *MNRAS*, 407, 2091
- Genzel, R., Newman, S., Jones, T., et al. 2011, *ApJ*, 733, 101
- Gnerucci, A., Marconi, A., Cresci, G., et al. 2011a, *A&A*, 528, A88
- Gnerucci, A., Marconi, A., Cresci, G., et al. 2011b, *A&A*, 533, A124
- Grazian, A., Fontana, A., de Santis, C., et al. 2006, *A&A*, 449, 951
- Grazian, A., Salimbeni, S., Pentericci, L., et al. 2007, *A&A*, 465, 393
- Hopkins, A. M., & Beacom, J. F. 2006, *ApJ*, 651, 142
- Hunt, L., Magrini, L., Galli, D., et al. 2012, *MNRAS*, 427, 906
- Jones, T., Ellis, R. S., Jullo, E., & Richard, J. 2010, *AJ*, 725, L176
- Jones, T., Ellis, R. S., Richard, J., & Jullo, E. 2013, *ApJ*, 765, 48

- Kennicutt, R. C. Jr. 1998, *ApJ*, 498, 541
 Kewley, L. J. 2006, AAS/AAPT Joint Meeting 209, BAAS, 38, 1221
 Kewley, L. J., & Ellison, S. L. 2008, *AJ*, 681, 1183
 Kewley, L. J., Dopita, M. A., Leitherer, C., et al. 2013, *AJ*, 774, 100
 Kneib, J.-P., Ellis, R. S., Smail, I., et al. 1996, *ApJ*, 471, 643
 Kobayashi, C., Springel, V., & White, S. D. M. 2007, *MNRAS*, 376, 1465
 Köppen, J., Weidner, C., & Kroupa, P. 2007, *MNRAS*, 375, 673
 Lagos, C. P., Baugh, C. M., & Lacey, C. G. 2011, *MNRAS*, 418, L1649
 Lara-Lopez, M., Cepa, J., Bongiovanni, A. et al. 2010, *A&A*, 521, L53
 Law, D. R., Steidel, C. C., Erb, D. K., et al. 2009, *ApJ*, 697, 2057
 Lehnert, M. D., Nesvadba, N. P. H., Le Tiran, L., et al. 2009, *ApJ*, 699, 1660
 Lilly, S. J., Carollo, C. M., Pipino, A., et al. 2013, *ApJ*, 772, 119
 Limousin, M., Richard, J., Jullo, E., et al. 2007, *ApJ*, 668, 643
 Maiolino, R., Nagao, T., Grazian, A., et al. 2008, *A&A*, 488, 463
 Maiolino, R., Gallerani, S., Neri, R., et al. 2012, *MNRAS*, 425, L66
 Magdis, G. E., Georgios, E., Daddi, E., et al. 2012a, *ApJ*, 758, L9
 Magdis, G. E., Daddi, E., Béthermin, M., et al. 2012b, *ApJ*, 760, 6
 Mannucci, F., Cresci, G., Maiolino, R., et al. 2009, *MNRAS*, 398, 1915
 Mannucci, F., Cresci, G., Maiolino, R., et al. 2010, *MNRAS*, 408, 2115
 Mannucci, F., Salvaterra, R., & Campisi, M. A. 2011, *MNRAS*, 414, 1263
 Maraston, C. 2005, *MNRAS*, 362, 799 (M05)
 Moller, P., Fynbo, J. P. U., Ledoux, C., & Nilsson, K. K. 2013, *MNRAS*, 430, 2680
 Mott, A., Spitoni, E., & Matteucci, F. 2013, *MNRAS*, 435, 2918
 Nilsson, K. K., & Moller, P. 2009, *A&A*, 508, L21
 Nilsson, K. K., & Moller, P. 2011, *A&A*, 527, L7
 Newman, S. F., Sarah, F., Genzel, R., et al. 2012, *ApJ*, 761, 43
 Obreschkow, D., & Rawlings, S. 2009, *AJ*, 696, L129
 Perez, J., Michel-Dansac, L., & Tissera, P. B. 2011, *MNRAS*, 417, 580
 Pérez-González, P. G., Rieke, G. H., Villar, V., et al. 2008, *ApJ*, 675, 234
 Pérez-Montero, E., Contini, T., Lamareille, F., et al. 2013, *A&A*, 549, A25
 Pilkington, K., Few, C. G., Gibson, B. K., et al. 2012, *A&A*, 540, A56
 Pozzetti, L., Bolzonella, M., Lamareille, F., et al. 2007, *A&A*, 474, 443
 Prochaska, J. X., & Wolfe, A. M., 2009, *ApJ*, 696, 1543
 Queyrel, J., Contini, T., Kissler-Patig, M., et al. 2012, *A&A*, 539, A93
 Reddy, N. A., Pettini, M., Steidel, C. C., et al. 2012, *ApJ*, 754, 25
 Richard, J., Jones, T., Ellis, R., et al. 2011, *MNRAS*, 413, 643
 Riechers, D., Carilli, C. L., Walter, F., & Momjian, E. 2010, *ApJ*, 724, 153
 Rupke, D. S. N., & Veilleux, S. 2011, *ApJ*, 729, L27
 Rupke, D. S. N., Kewley, L. J., & Chien, L.-H. 2010, *ApJ*, 723, 1255
 Sakstein, J., Pipino, A., Devriendt, J. E. G., & Maiolino, R. 2011, *MNRAS*, 410, 2203
 Saintonge, A., Kauffmann, G., Kramer, C., et al. 2011, *MNRAS*, 415, 32
 Saintonge, A., Lutz, D., Genzel, R., et al. 2013, *ApJ*, 778, 2
 Santini, P., Maiolino, R., Magnelli, B., et al. 2014, *A&A*, 562, A30
 Sánchez, S. F., Rosales-Ortega, F. F., Jungwiert, B. et al. 2013, *A&A*, 554, A58
 Schrubba, P., Leroy, A. K., Walter, F., et al. 2011, *AJ*, 142, 37
 Smail, I., Swinbank, A. M., Richard, J., et al. 2007, *AJ*, 654, L33
 Schmidt, M. 1959, *ApJ*, 129, 243
 Sommariva, V., Mannucci, F., Cresci, G., et al. 2012, *A&A*, 539, A136
 Steidel, C. C., Adelberger, K. L., Shapley, A. E., et al. 2003, *ApJ*, 592, 728
 Steidel, C. C., Erb, D. K., Shapley, A. E., et al. 2010, *ApJ*, 717, 289
 Sturm, E., González-Alfonso, E., Veilleux, S., et al. 2011, *ApJ*, 733, L16
 Tacconi, L. J., Genzel, R., Neri, R., et al. 2010, *Nature*, 463, 781
 Tacconi, L. J., Neri, R., Genzel, R., et al. 2013, *ApJ*, 768, 74
 Tan, Q., Daddi, E., Sargent, M., et al. 2013, *ApJ*, 776, 24
 Torrey, P., Cox, T. J., Kewley, L., & Hernquist, L. 2012, *ApJ*, 746, 108
 Tremonti, C. A., Heckman, T. M., Kauffmann, G., et al. 2004, *ApJ*, 613, 898
 van de Voort, F., Schaye, J., Altay, G., & Theuns, T. 2012, *MNRAS*, 421, 2809
 Vanzella, E., Cristiani, S., Dickinson, M., et al. 2006, *A&A*, 454, 423
 Vergani, D., Epinat, B., Contini, T., et al. 2012, *A&A*, 546, A118
 Yates, R. M., Kauffmann, G., & Guo, Q. 2012, *MNRAS*, 422, 215
 Yuan, T.-T., Kewley, L. J., & Rich, J. 2013, *ApJ*, 767, 106

Appendix A: Integrated near-IR spectra of the AMAZE and LSD galaxies

Figures A.1–A.4 show the integrated spectra of all galaxies in the AMAZE and LSD samples, restricted to the spectral regions that cover the nebular lines used to measure the metallicities.

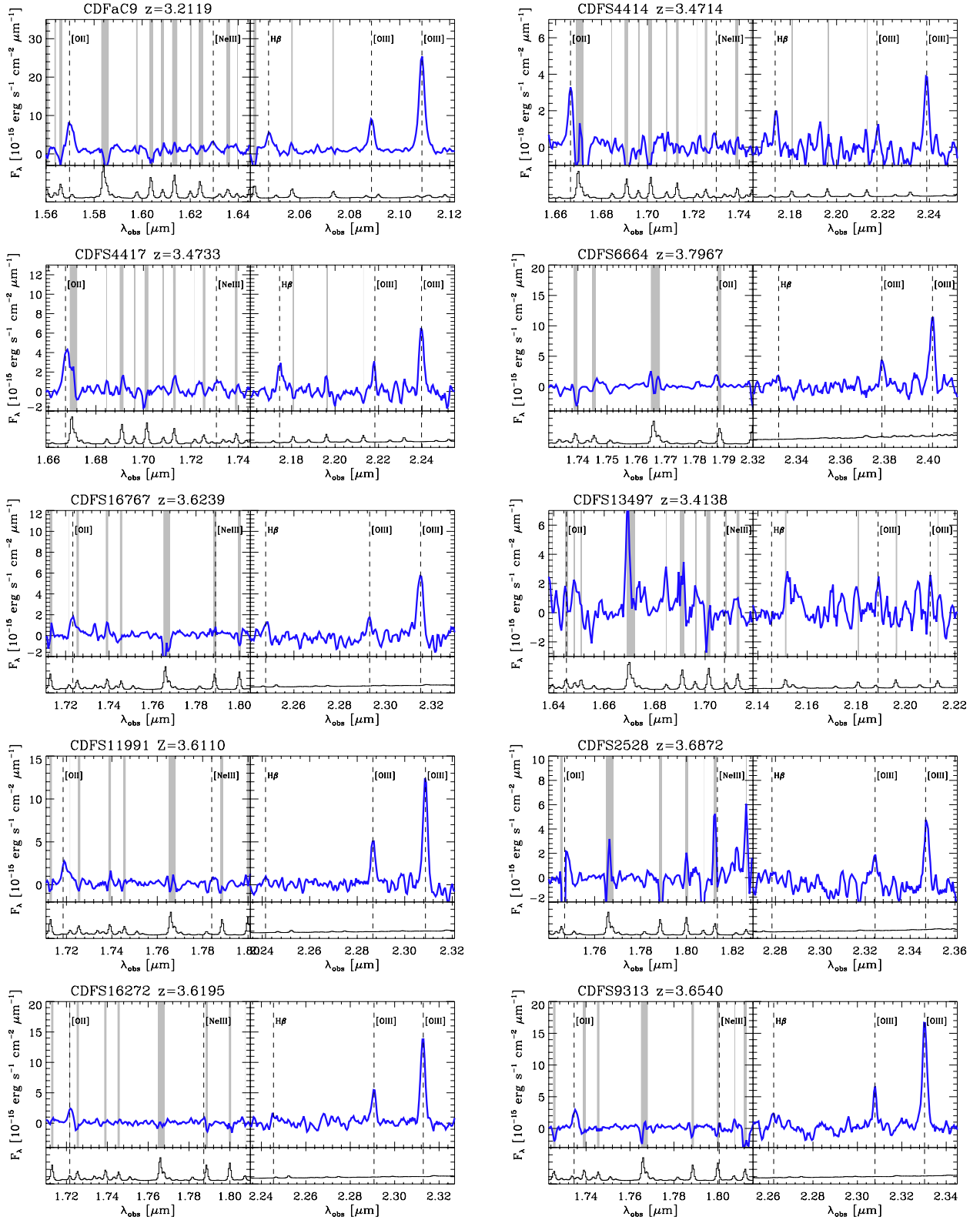


Fig. A.1. Near-IR spectra of the galaxies in the AMAZE sample. The vertical dashed lines indicate the expected location of nebular emission lines. The shaded vertical regions overlaid on each spectrum highlight spectral regions affected by strong sky emission lines.

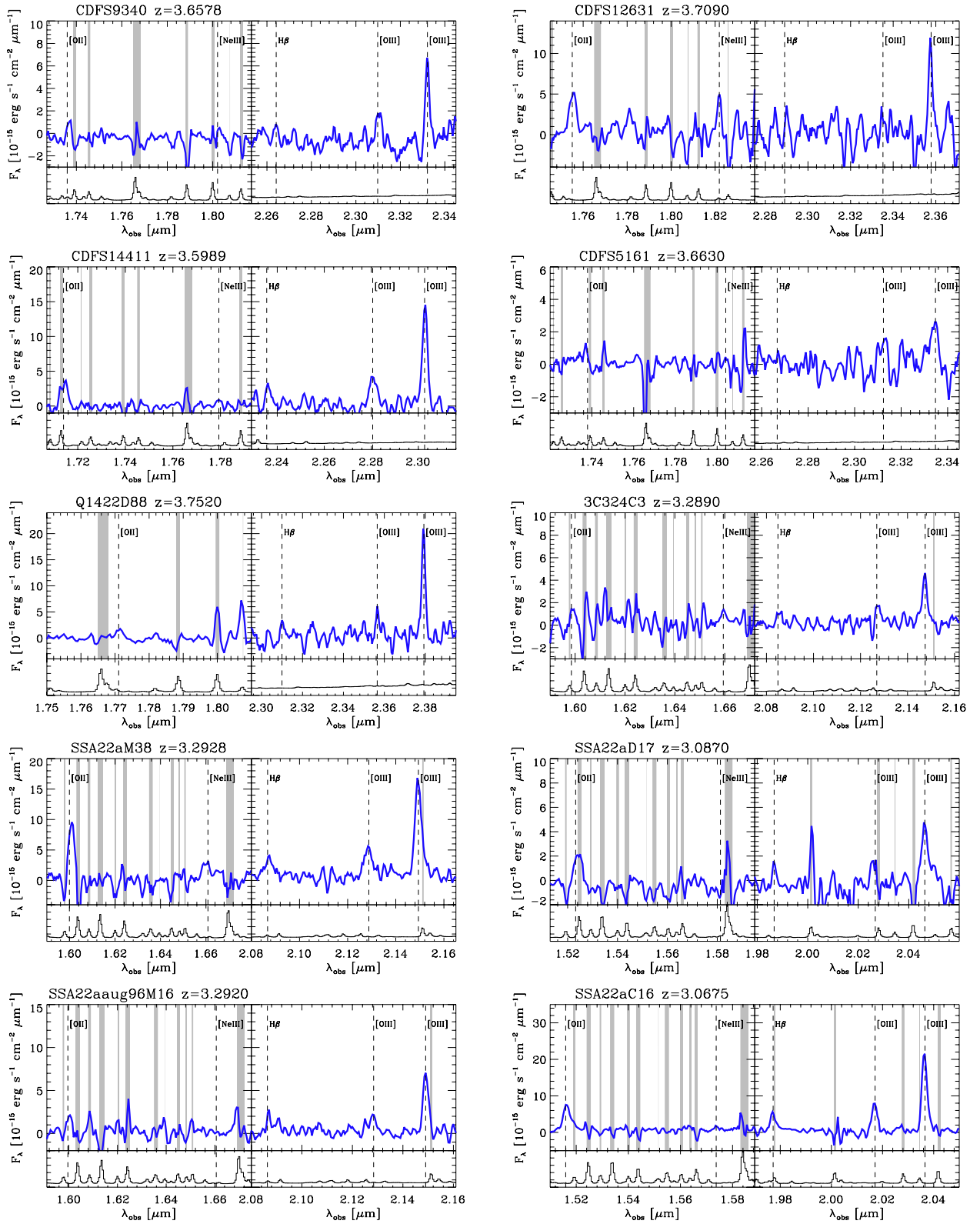


Fig. A.2. Near-IR spectra of the galaxies in the AMAZE sample. The vertical dashed lines indicate the expected location of nebular emission lines. The shaded vertical regions overlaid on each spectrum highlight spectral regions affected by strong sky emission lines.

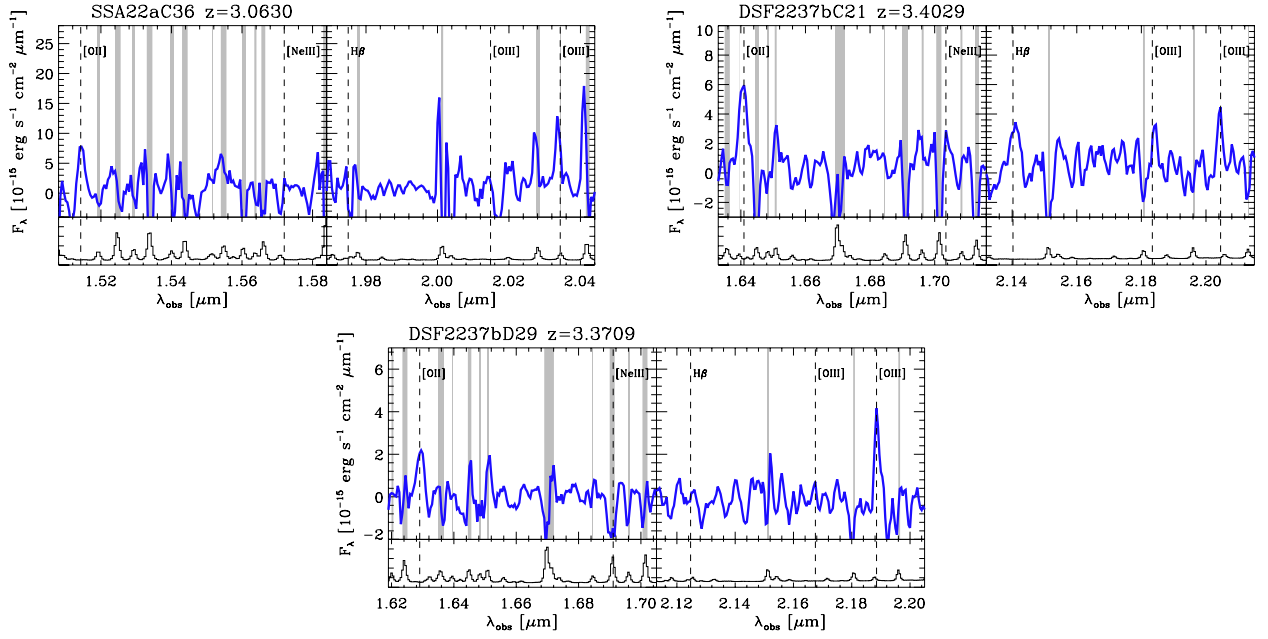


Fig. A.3. Near-IR spectra of the galaxies in the AMAZE sample. The vertical dashed lines indicate the expected location of nebular emission lines. The shaded vertical regions overlaid on each spectrum highlight spectral regions affected by strong sky emission lines.

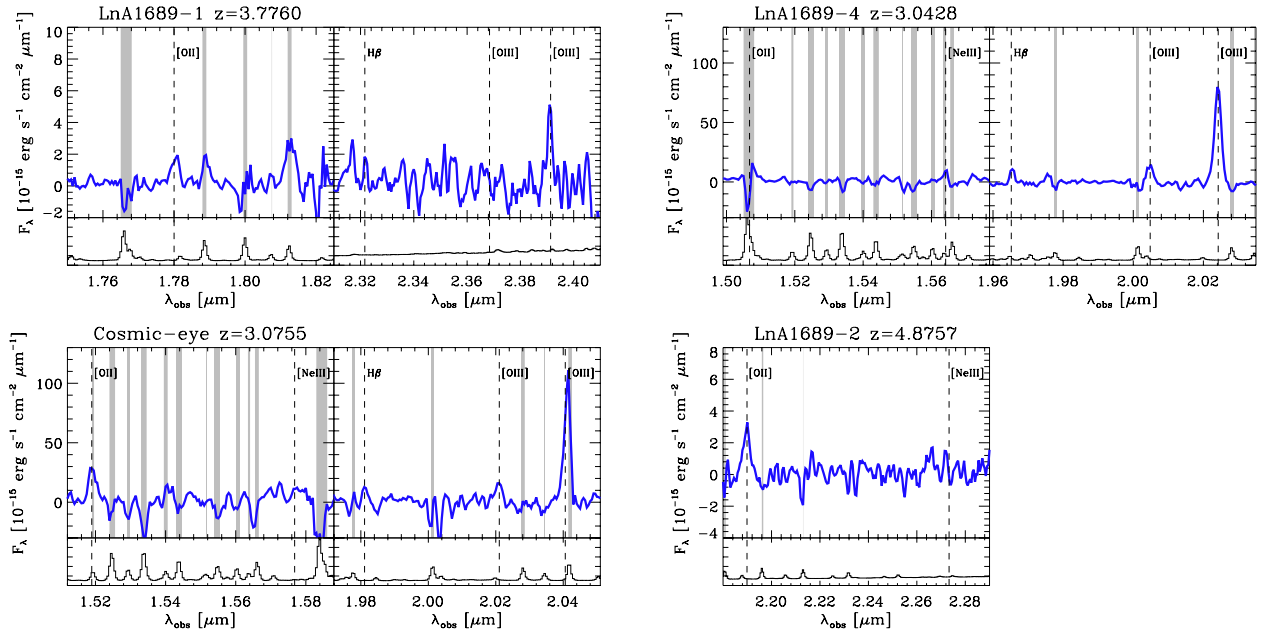


Fig. A.4. Near-IR spectra of the lensed galaxies in the AMAZE sample. The vertical dashed lines indicate the expected location of nebular emission lines. The shaded vertical regions overlaid on each spectrum highlight spectral regions affected by strong sky emission lines.

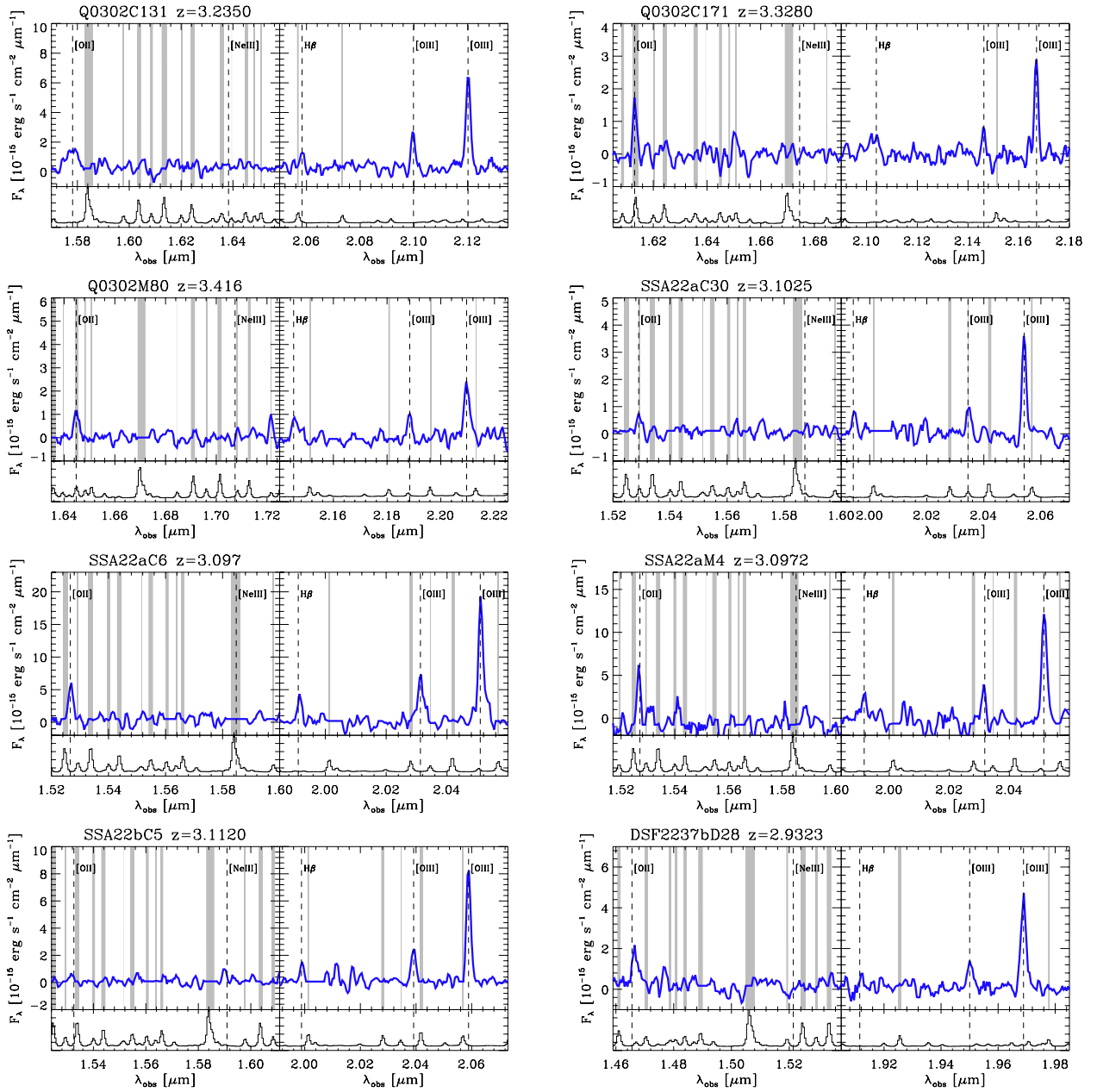


Fig. A.5. Near-IR spectra of the galaxies in the LSD sample. The vertical dashed lines indicate the expected location of nebular emission lines. The shaded vertical regions overlaid on each spectrum highlight spectral regions affected by strong sky emission lines.

Appendix B: Metallicity measurements

In this appendix we provide some additional details on the measurements of the gas metallicity. As mentioned in Sect. 5, the metallicities were inferred following the calibrations and the method described in detail in Maiolino et al. (2008). Here we briefly summarize the method and show the application to our full sample of galaxies. Maiolino et al. (2008) inferred the relationship between metallicity and various nebular line ratios by exploiting a combination of direct measurements (based on the T_e method, mostly at low metallicities) and photoionization modeling (mostly at high metallicities). It has recently been argued that the excitation conditions in high- z galaxies are different from the local ones and that, therefore, the local calibrations may not apply to high redshift (Kewley et al. 2013). However, we found in a parallel work (Maiolino et al., in prep) that local calibrations are indeed appropriate for high- z galaxies, after selection effects are properly taken in to account. These relations are shown in Fig. B.1, where solid black lines show the average of the galaxy distribution and the dashed black lines show the dispersion. Each of these diagnostics has advantages and disadvantages. Some of them are practically unaffected by extinction (e.g., [OIII]/H β), but have a double-degenerate metallicity solution; others have a monotonic dependence on metallicity (e.g., [OIII]/[OII], [NeIII]/[OII]), but have high dispersion and are affected by reddening. However, when these diagnostics are used simultaneously, only some combinations of metallicity and reddening are allowed by the data. Obviously, not all of the diagnostics shown in Figs. B.1–B.5 are independent.

We decided to use the following independent metallicity diagnostics: R_{23} (which has the tightest relationship with metallicity, although with double solution), [OIII]/[OII] (which has a monotonic dependence on metallicity, although with large scatter, which allowed us to remove the degeneracy on R_{23}), and, when available, [NeIII]/[OII] (which also has a monotonic dependence on metallicity). In practice, we determined the χ^2 for each combination of metallicity and dust extinction for each of these relations, and found the best combination as the minimum of χ^2 .

The result of this method is shown, for each object in our sample, in Figs. B.1–B.5. The upper-left panel of the figure associated with each object shows in the metallicity-extinction plane the best-fitting value (blue cross) and the 1σ confidence level. Clearly, the metallicity is generally well constrained. The extinction is instead poorly constrained by this method; but this figure shows us that the uncertainties on extinction do not significantly affect the metallicity determination. In the other panels the vertical green error bar indicates the measured ratio with the associated uncertainties, while the blue cross gives the best-fit value of the metallicity and the dereddened ratio assuming the best-fit reddening value; the red lines show the projection of the 1σ confidence levels. The horizontal green error bar shows the resulting uncertainty on the metallicity.

While Figs. B.1–B.5 only show the results for the line ratios obtained from the integrated fluxes in each galaxy, the same method was applied pixel-to-pixel for resolved galaxies to infer the metallicity maps shown in Figs. 11–13.

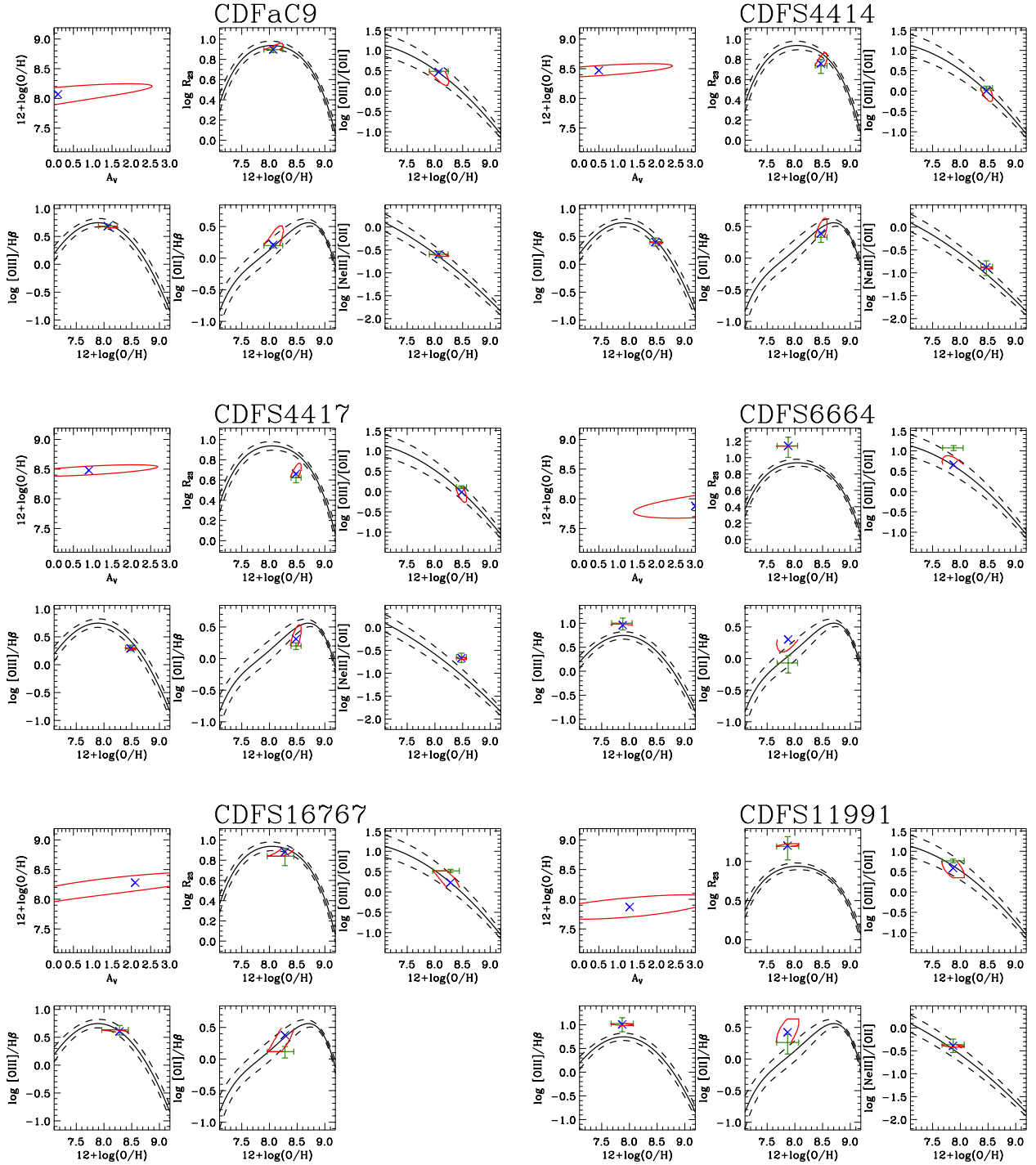


Fig. B.1. Diagnostic tools used to determine the metallicity of galaxies in the AMAZE sample. In each block, the *top-left* panel shows the best solution (blue cross) and the 1σ confidence level in the A_V -metallicity plane. In the *other panels* the solid black line (best fit) and the dashed lines (dispersion) show the empirical relations between various line ratios and the gas metallicity. The green error bars show the observed ratios (along the y -axis) and the best-fit metallicity with uncertainty (along the x -axis); the blue cross shows the de-reddened ratios from adopting the best-fit extinction; the red line shows the projection of the 1σ uncertainty of the fit in the *top-left* panel.

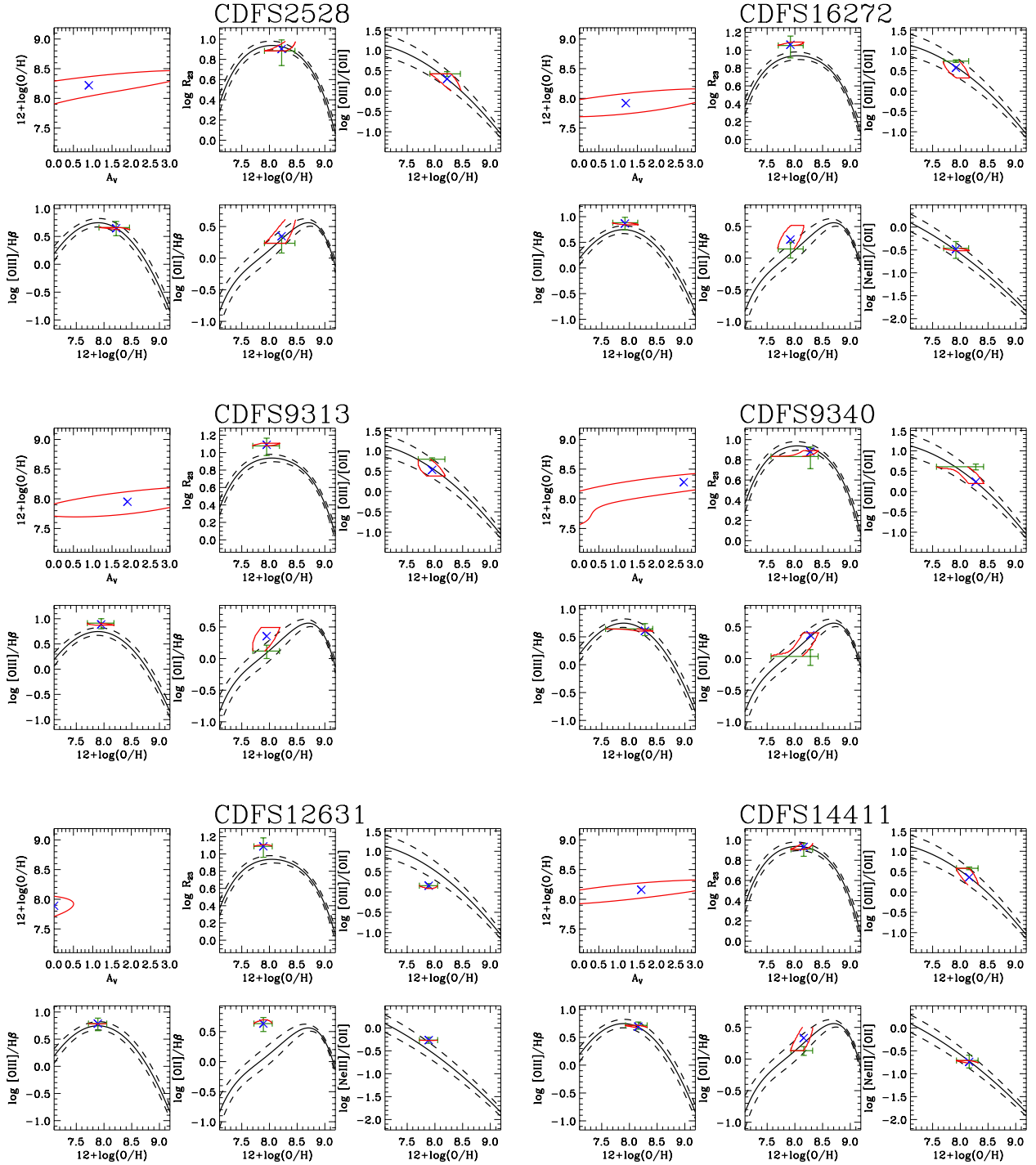


Fig. B.2. Diagnostic tools used to determine the metallicity of the galaxies in the AMAZE sample. In each block, the *top-left* panel shows the best solution (blue cross) and the 1σ confidence level in the A_V -metallicity plane. In the *other panels* the solid black line (best fit) and the dashed lines (dispersion) show the empirical relations between various line ratios and the gas metallicity. The green error bars show the observed ratios (along the y -axis) and the best-fit metallicity with uncertainty (along the x -axis); the blue cross shows the de-reddened ratios from adopting the best-fit extinction; the red line shows the projection of the 1σ uncertainty of the fit in the *top-left* panel.

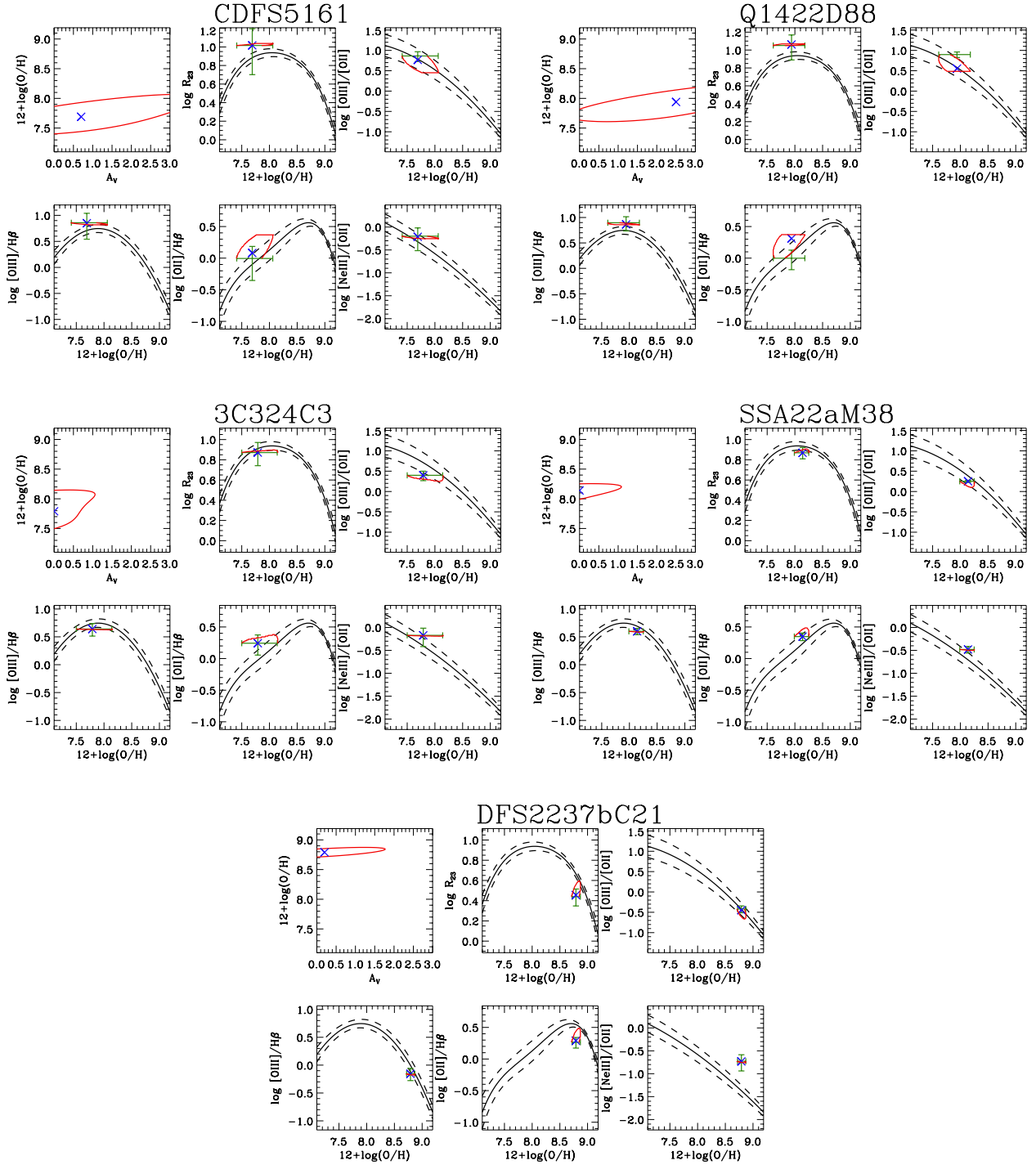


Fig. B.3. Diagnostic tools used to determine the metallicity of the galaxies in the AMAZE sample. In each block, the *top-left panel* shows the best solution (blue cross) and the 1σ confidence level in the A_V -metallicity plane. In the *other panels* the solid black line (best fit) and the dashed lines (dispersion) show the empirical relations between various line ratios and the gas metallicity. The green error bars show the observed ratios (along the y -axis) and the best-fit metallicity with uncertainty (along the x -axis); the blue cross shows the de-reddened ratios from adopting the best-fit extinction; the red line shows the projection of the 1σ uncertainty of the fit in the *top-left panel*.

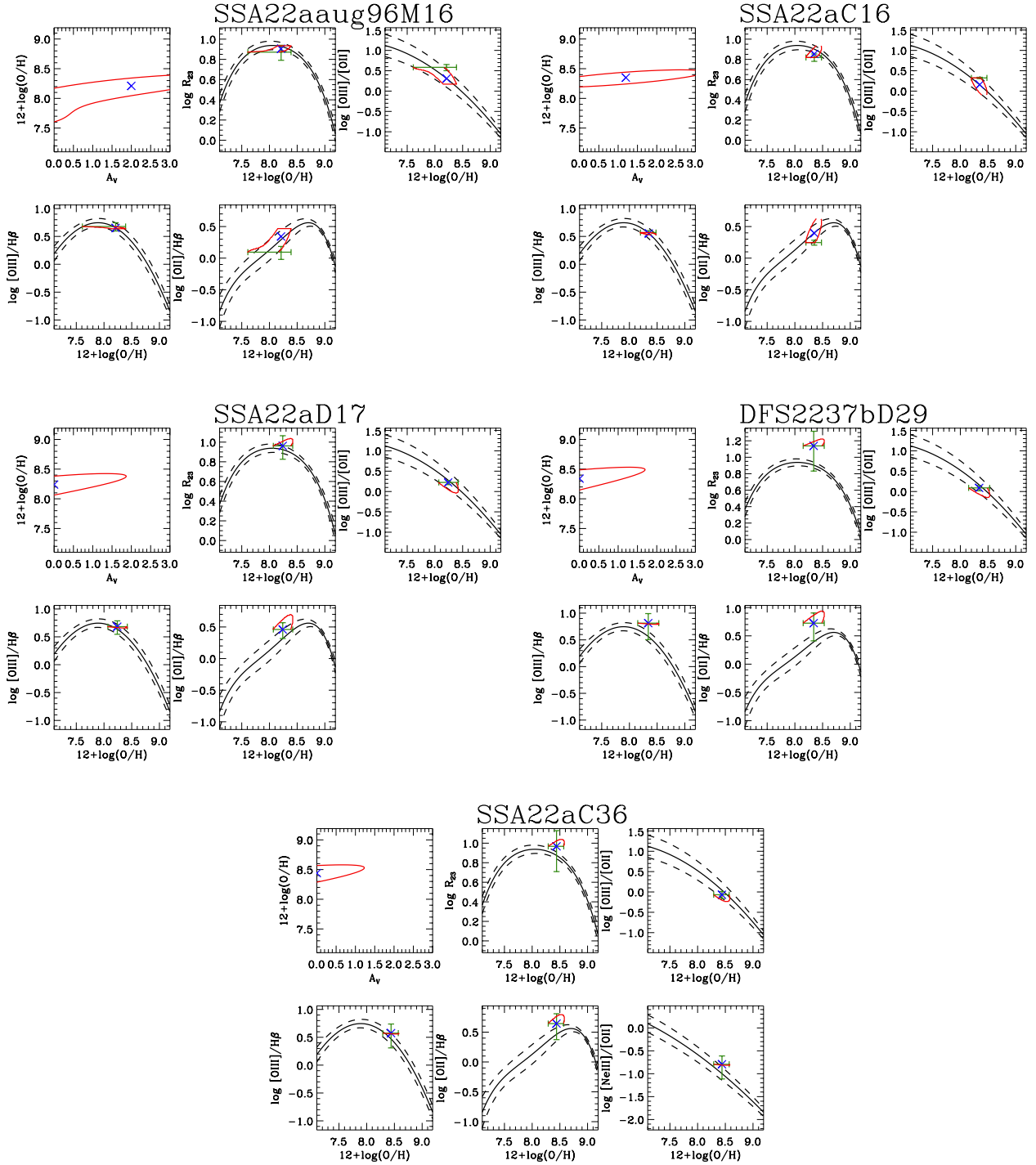


Fig. B.4. Diagnostic tools used to determine the metallicity of the galaxies in the AMAZE sample. In each block, the *top-left panel* shows the best solution (blue cross) and the 1σ confidence level in the A_V -metallicity plane. In *the other panels* the solid black line (best fit) and the dashed lines (dispersion) show the empirical relations between various line ratios and the gas metallicity. The green error bars show the observed ratios (along the y -axis) and the best-fit metallicity with uncertainty (along the x -axis); the blue cross shows the de-reddened ratios from adopting the best-fit extinction; the red line shows the projection of the 1σ uncertainty of the fit in the *top-left panel*.

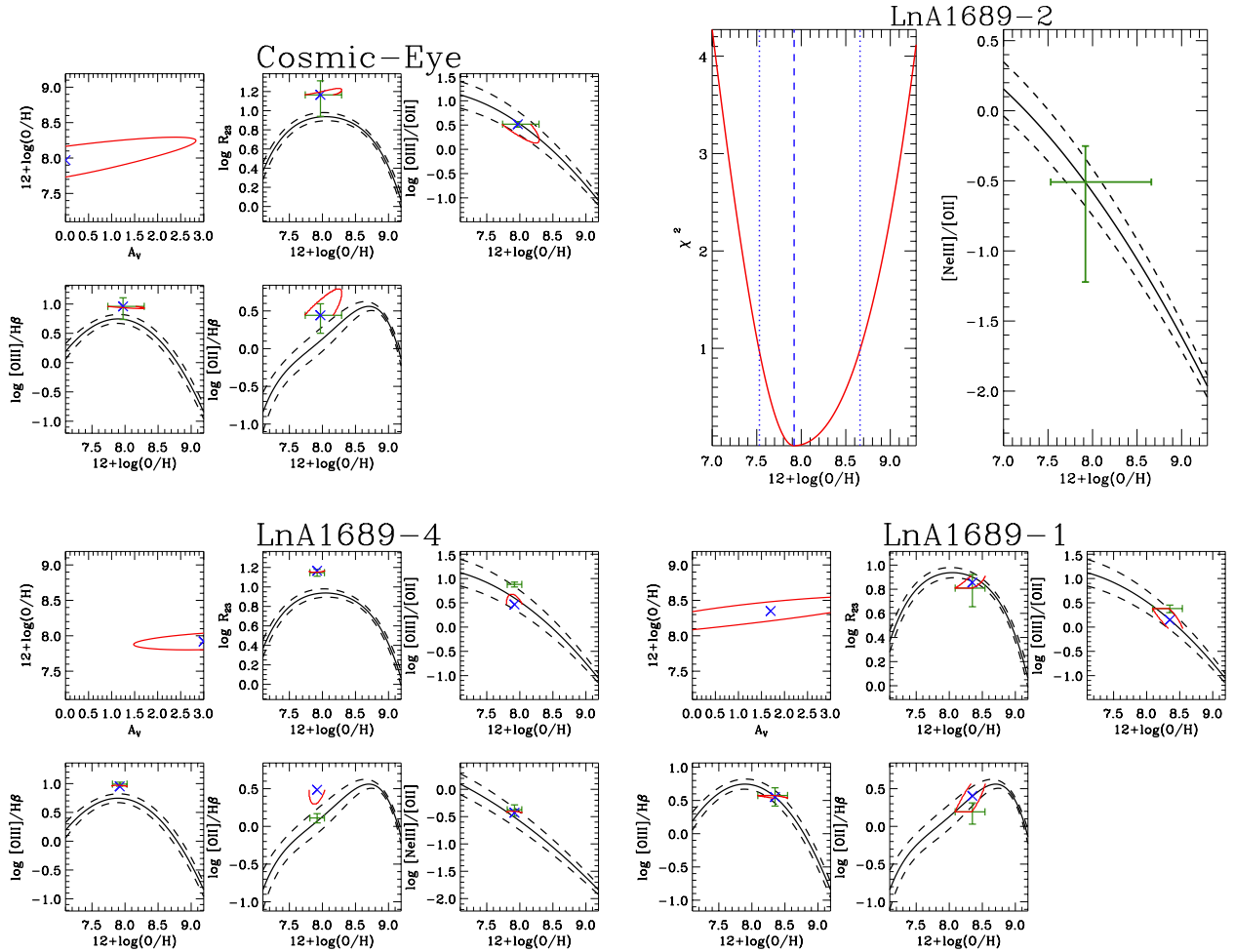


Fig. B.5. Diagnostic tools used to determine the metallicity of lensed galaxies in the AMAZE sample. In each block, the *top-left panel* shows the best solution (blue cross) and the 1σ confidence level in the A_V –metallicity plane. In *the other panels* the solid black line show the average relations between various line ratios and the gas metallicity as inferred by [Maiolino et al. \(2008\)](#). The dashed lines show the associated dispersions. The green error bars show the observed ratios (along the y -axis) and the best-fit metallicity with uncertainty (along the x -axis); the blue cross shows the best-fit metallicity and the de-reddened ratios from adopting the best-fit extinction; the red line shows the projection of the 1σ uncertainty of the fit in the *top-left panel*. For the lensed AMAZE galaxy LnA1689-2 the metallicity was inferred from the [NeIII]/[OII] line ratio exploiting the anticorrelation (though with high dispersion) between this line ratio and the metallicity found in [Maiolino et al. \(2008\)](#).